

## Euclid

### I. Overview of the *Euclid* mission★

Euclid Collaboration: Y. Mellier<sup>1,2,★★</sup>, Abdurro'uf<sup>3</sup>, J. A. Acevedo Barroso<sup>4</sup>, A. Achúcarro<sup>5,6</sup>, J. Adamek<sup>7</sup>, R. Adam<sup>8</sup>, G. E. Addison<sup>3</sup>, N. Aghanim<sup>9</sup>, M. Aguena<sup>10</sup>, V. Ajani<sup>11,12,13</sup>, Y. Akrami<sup>14,15</sup>, A. Al-Bahlawan<sup>16</sup>, A. Alavi<sup>17</sup>, I. S. Albuquerque<sup>18</sup>, G. Alestas<sup>14</sup>, G. Alguero<sup>19</sup>, A. Allaoui<sup>20</sup>, S. W. Allen<sup>21,22,23</sup>, V. Allevaro<sup>24</sup>, A. V. Alonso-Tetilla<sup>25</sup>, B. Altieri<sup>26</sup>, A. Alvarez-Candal<sup>27,28</sup>, S. Alvi<sup>29</sup>, A. Amara<sup>30</sup>, L. Amendola<sup>31</sup>, J. Amiaux<sup>11</sup>, I. T. Andika<sup>32,33</sup>, S. Andreon<sup>34</sup>, A. Andrews<sup>35</sup>, G. Angora<sup>24,29</sup>, R. E. Angulo<sup>36,37</sup>, F. Annibali<sup>35</sup>, A. Anselmi<sup>38</sup>, S. Anselmi<sup>39,40,41</sup>, S. Arcari<sup>29,42</sup>, M. Archidiacono<sup>43,44</sup>, G. Arico<sup>7</sup>, M. Arnaud<sup>45,46</sup>, S. Arnouts<sup>20</sup>, M. Asgari<sup>47</sup>, J. Asorey<sup>48</sup>, L. Atayde<sup>18</sup>, H. Atek<sup>2</sup>, F. Atrio-Barandela<sup>49</sup>, M. Aubert<sup>50,51</sup>, E. Aubourg<sup>10,45</sup>, T. Auphan<sup>52</sup>, N. Auricchio<sup>35</sup>, B. Aussel<sup>53</sup>, H. Aussel<sup>11</sup>, P. P. Avelino<sup>54,55</sup>, A. Avgoustidis<sup>56</sup>, S. Avila<sup>57</sup>, S. Awan<sup>16</sup>, R. Azzollini<sup>16</sup>, C. Baccigalupi<sup>58,59,60,61</sup>, E. Bachelet<sup>62</sup>, D. Bacon<sup>63</sup>, M. Baes<sup>64</sup>, M. B. Bagley<sup>65</sup>, B. Bahr-Kalus<sup>51,66</sup>, A. Balaguera-Antolinez<sup>67,68</sup>, E. Balbinot<sup>69,70</sup>, M. Balcells<sup>67,68,71</sup>, M. Baldi<sup>72,35,73</sup>, I. Baldry<sup>74</sup>, A. Balestra<sup>75</sup>, M. Ballardini<sup>29,35,42</sup>, O. Ballester<sup>57</sup>, M. Balogh<sup>76,77</sup>, E. Bañados<sup>78</sup>, R. Barbier<sup>51</sup>, S. Bardelli<sup>35</sup>, M. Baron<sup>51</sup>, T. Barreiro<sup>18,79</sup>, R. Barrena<sup>80</sup>, J.-C. Barriere<sup>81</sup>, B. J. Barros<sup>18</sup>, A. Barthelemy<sup>82</sup>, N. Bartolo<sup>40,39,75</sup>, A. Basset<sup>83</sup>, P. Battaglia<sup>35</sup>, A. J. Battisti<sup>84,85,86</sup>, C. M. Baugh<sup>87</sup>, L. Baumont<sup>11</sup>, L. Bazzanini<sup>29,35</sup>, J.-P. Beaulieu<sup>1,88</sup>, V. Beckmann<sup>89</sup>, A. N. Belikov<sup>69,90</sup>, J. Bel<sup>91</sup>, F. Bellagamba<sup>72,35</sup>, M. Bella<sup>92</sup>, E. Bellini<sup>61,58,59,60</sup>, K. Benabed<sup>2</sup>, R. Bender<sup>93,82</sup>, G. Benevento<sup>94</sup>, C. L. Bennett<sup>3</sup>, K. Benson<sup>16</sup>, P. Bergamini<sup>43,35</sup>, J. R. Bermejo-Cliant<sup>67,68</sup>, F. Bernardeau<sup>95,2</sup>, D. Bertacca<sup>40,75,39</sup>, M. Berthe<sup>11</sup>, J. Berthier<sup>96</sup>, M. Bethermin<sup>97,20</sup>, F. Beutler<sup>98</sup>, C. Bevilion<sup>99</sup>, S. Bhargava<sup>100</sup>, R. Bhatawdekar<sup>26</sup>, D. Bianchi<sup>43</sup>, L. Bisigello<sup>101,40</sup>, A. Biviano<sup>59,58</sup>, R. P. Blake<sup>98</sup>, A. Blanchard<sup>92</sup>, J. Blazek<sup>102</sup>, L. Blot<sup>103,41</sup>, A. Bosco<sup>38</sup>, C. Bodendorf<sup>93</sup>, T. Boenke<sup>104</sup>, H. Böhringer<sup>93,105,106</sup>, P. Boldrini<sup>2</sup>, M. Bolzonella<sup>35</sup>, A. Bonchi<sup>107</sup>, M. Bonici<sup>108,77,109</sup>, D. Bonino<sup>110</sup>, L. Bonino<sup>38</sup>, C. Bonvin<sup>111</sup>, W. Bon<sup>20</sup>, J. T. Booth<sup>112</sup>, S. Borgani<sup>113,58,59,60</sup>, A. S. Borlaff<sup>114,115</sup>, E. Borsato<sup>40,39</sup>, A. Bosco<sup>38</sup>, B. Bose<sup>98</sup>, M. T. Botticella<sup>24</sup>, A. Boucaud<sup>10</sup>, F. Bouche<sup>116,117</sup>, J. S. Boucher<sup>16</sup>, D. Boutigny<sup>118</sup>, T. Bouvard<sup>119</sup>, R. Bouwens<sup>70</sup>, H. Bouy<sup>120,121</sup>, R. A. A. Bowler<sup>122</sup>, V. Bozza<sup>123,124</sup>, E. Bozzo<sup>125</sup>, E. Branchini<sup>126,127,34</sup>, G. Brando<sup>128</sup>, S. Brau-Nogue<sup>92</sup>, P. Brekke<sup>129</sup>, M. N. Bremer<sup>130</sup>, M. Brescia<sup>131,24,117</sup>, M.-A. Breton<sup>132,133,41</sup>, J. Brinchmann<sup>55</sup>, T. Brinckmann<sup>29,42</sup>, C. Brockley-Blatt<sup>16</sup>, M. Brodwin<sup>134</sup>, L. Brouard<sup>99</sup>, M. L. Brown<sup>122</sup>, S. Bruton<sup>135</sup>, J. Bucko<sup>7,12</sup>, H. Buddelmeijer<sup>69,70</sup>, G. Buenadicha<sup>26</sup>, F. Buitrago<sup>136,137</sup>, P. Burger<sup>138,77</sup>, C. Burigana<sup>101,139</sup>, V. Busillo<sup>24,131,117</sup>, D. Busonero<sup>110</sup>, R. Cabanac<sup>92</sup>, L. Cabayol-Garcia<sup>57,140</sup>, M. S. Cagliari<sup>43</sup>, A. Caillat<sup>20</sup>, L. Caillat<sup>52</sup>, M. Calabrese<sup>141,108</sup>, A. Calabro<sup>142</sup>, G. Calderone<sup>59</sup>, F. Calura<sup>35</sup>, B. Camacho Quevedo<sup>143,132</sup>, S. Camera<sup>144,13,110</sup>, L. Campos<sup>104</sup>, G. Cañas-Herrera<sup>104,5</sup>, G. P. Candini<sup>16</sup>, M. Cantiello<sup>145</sup>, V. Capobianco<sup>110</sup>, E. Cappellaro<sup>75</sup>, N. Cappelluti<sup>146</sup>, A. Cappi<sup>35,8</sup>, K. I. Caputi<sup>69,147</sup>, C. Cara<sup>11</sup>, C. Carbone<sup>108</sup>, V. F. Cardone<sup>142,148</sup>, E. Carella<sup>108,43</sup>, R. G. Carlberg<sup>149</sup>, M. Carle<sup>20</sup>, L. Carminati<sup>99</sup>, F. Caro<sup>142</sup>, J. M. Carrasco<sup>150,151,143</sup>, J. Carretero<sup>152,140</sup>, P. Carrilho<sup>98</sup>, J. Carron Duque<sup>14</sup>, B. Carry<sup>8</sup>, A. Carvalho<sup>153,18</sup>, C. S. Carvalho<sup>137</sup>, R. Casas<sup>143,132</sup>, S. Casas<sup>154</sup>, P. Casenove<sup>83</sup>, C. M. Casey<sup>65,147</sup>, P. Cassata<sup>40,75</sup>, F. J. Castander<sup>132,143</sup>, D. Castela<sup>18</sup>, M. Castellano<sup>142</sup>, L. Castiblanco<sup>47,155</sup>, G. Castignani<sup>35</sup>, T. Castro<sup>59,60,58,156</sup>, C. Cavet<sup>10</sup>, S. Cavuoti<sup>24,117</sup>, P.-Y. Chabaud<sup>20</sup>, K. C. Chambers<sup>157</sup>, Y. Charles<sup>20</sup>, S. Charlot<sup>2</sup>, N. Chartab<sup>158</sup>, R. Chary<sup>17</sup>, F. Chaumeil<sup>99</sup>, H. Cho<sup>112</sup>, G. Chon<sup>105,106</sup>, E. Ciancetta<sup>38</sup>, P. Ciliegi<sup>35</sup>, A. Cimatti<sup>159</sup>, M. Cimino<sup>104</sup>, M.-R. L. Cioni<sup>160</sup>, R. Claydon<sup>98</sup>, C. Cleland<sup>10</sup>, B. Clément<sup>4,161</sup>, D. L. Clements<sup>162</sup>, N. Clerc<sup>92</sup>, S. Clesse<sup>163</sup>, S. Codis<sup>11</sup>, F. Cogato<sup>164,35</sup>, J. Colbert<sup>17</sup>, R. E. Cole<sup>16</sup>, P. Coles<sup>165</sup>, T. E. Collett<sup>63</sup>, R. S. Collins<sup>98</sup>, C. Colodro-Conde<sup>67</sup>, C. Colombo<sup>104</sup>, F. Combes<sup>166,167</sup>, V. Conforti<sup>35</sup>, G. Congedo<sup>98</sup>, S. Conseil<sup>51</sup>, C. J. Conselice<sup>122</sup>, S. Contarini<sup>93</sup>, T. Contini<sup>92</sup>, L. Conversi<sup>168,26</sup>, A. R. Cooray<sup>169</sup>,

★ Dedicated to our friends and colleagues Olivier Le Fèvre (1960–2020) and Nick Kaiser (1954–2023), who contributed so much to the *Euclid* mission and its underlying science.

★★ Corresponding author; mellier@iap.fr, hoekstra@strw.leidenuniv.nl

Y. Copin<sup>51</sup>, P.-S. Corasaniti<sup>41</sup>, P. Corcho-Caballero<sup>69</sup>, L. Corcione<sup>110</sup>, O. Cordes<sup>138</sup>, O. Corpacci<sup>81</sup>, M. Correnti<sup>142,107</sup>, M. Costanzi<sup>113,59,58</sup>, A. Costille<sup>20</sup>, F. Courbin<sup>4</sup>, L. Courcoul Mifsud<sup>99</sup>, H. M. Courtois<sup>66</sup>, M.-C. Cousinou<sup>52</sup>, G. Covone<sup>131,24,117</sup>, T. Cowell<sup>170</sup>, C. Cragg<sup>171</sup>, G. Cresci<sup>172</sup>, S. Cristiani<sup>59,60,58</sup>, M. Croce<sup>132,133</sup>, M. Cropper<sup>16</sup>, P. E. Crouzet<sup>104</sup>, B. Csizi<sup>173</sup>, J.-G. Cuby<sup>174,20</sup>, E. Cucchetti<sup>83</sup>, O. Cucciati<sup>35</sup>, J.-C. Cuillandre<sup>11</sup>, P. A. C. Cunha<sup>175,55</sup>, V. Cuzozzo<sup>176,94</sup>, E. Daddi<sup>11</sup>, M. D'Addona<sup>24,123</sup>, C. Dafonte<sup>177</sup>, N. Dagoneau<sup>178</sup>, E. Dalessandro<sup>35</sup>, G. B. Dalton<sup>171</sup>, G. D'Amico<sup>179,180</sup>, H. Dannerbauer<sup>181</sup>, P. Danto<sup>83</sup>, I. Das<sup>62</sup>, A. Da Silva<sup>153,18</sup>, R. da Silva<sup>142,107</sup>, W. d'Assignies Doumerg<sup>57</sup>, G. Daste<sup>20</sup>, J. E. Davies<sup>78</sup>, S. Davini<sup>127</sup>, P. Dayal<sup>69</sup>, T. de Boer<sup>157</sup>, R. Decarli<sup>35</sup>, B. De Caro<sup>108</sup>, H. Degaudenzi<sup>125</sup>, G. Degni<sup>182,183</sup>, J. T. A. de Jong<sup>70,69</sup>, L. F. de la Bella<sup>63</sup>, S. de la Torre<sup>20</sup>, F. Delhaise<sup>170</sup>, D. Delley<sup>93</sup>, G. Delucchi<sup>126,127</sup>, G. De Lucia<sup>59</sup>, J. Denniston<sup>16</sup>, F. De Paolis<sup>184,185,186</sup>, M. De Petris<sup>187,142</sup>, A. Derosa<sup>35</sup>, S. Desai<sup>188</sup>, V. Desjacques<sup>189</sup>, G. Despali<sup>164,35,73</sup>, G. Desprez<sup>190</sup>, J. De Vicente-Albendea<sup>152</sup>, Y. Deville<sup>92</sup>, J. D. F. Dias<sup>191,55,175</sup>, A. Díaz-Sánchez<sup>192</sup>, J. J. Diaz<sup>181</sup>, S. Di Domizio<sup>126,127</sup>, J. M. Diego<sup>193</sup>, D. Di Ferdinando<sup>73</sup>, A. M. Di Giorgio<sup>194</sup>, P. Dimauro<sup>142,195</sup>, J. Dinis<sup>153,18</sup>, K. Dolag<sup>82</sup>, C. Dolding<sup>16</sup>, H. Dole<sup>9</sup>, H. Domínguez Sánchez<sup>196</sup>, O. Doré<sup>197,112</sup>, F. Dournac<sup>92</sup>, M. Douspis<sup>9</sup>, H. Dreihahn<sup>170</sup>, B. Droge<sup>198</sup>, B. Dryer<sup>199</sup>, F. Dubath<sup>125</sup>, P.-A. Duc<sup>97</sup>, F. Ducret<sup>20</sup>, C. Duffy<sup>200</sup>, F. Dufresne<sup>20</sup>, C. A. J. Duncan<sup>122</sup>, X. Dupac<sup>26</sup>, V. Duret<sup>52</sup>, R. Durrer<sup>111</sup>, F. Durret<sup>1</sup>, S. Dusini<sup>39</sup>, A. Ealet<sup>51</sup>, A. Eggemeier<sup>138</sup>, P. R. M. Eisenhardt<sup>112</sup>, D. Elbaz<sup>11</sup>, M. Y. Elkhachab<sup>39,40</sup>, A. Ellien<sup>100</sup>, J. Endicott<sup>201</sup>, A. Enia<sup>72,35</sup>, T. Erben<sup>138</sup>, J. A. Escartin Vigo<sup>93</sup>, S. Escoffier<sup>52</sup>, I. Escudero Sanz<sup>104</sup>, J. Essert<sup>170</sup>, S. Etori<sup>35,139</sup>, M. Ezziati<sup>20</sup>, G. Fabbian<sup>202,203</sup>, M. Fabricius<sup>93,82</sup>, Y. Fang<sup>82</sup>, A. Farina<sup>126,34,127</sup>, M. Farina<sup>194</sup>, R. Farinelli<sup>35</sup>, S. Farrens<sup>11</sup>, F. Faustini<sup>107,142</sup>, A. Feltre<sup>172</sup>, A. M. N. Ferguson<sup>98</sup>, P. Ferrando<sup>11</sup>, A. G. Ferrari<sup>159,73</sup>, A. Ferré-Mateu<sup>68,67</sup>, P. G. Ferreira<sup>171</sup>, I. Ferreras<sup>204,67,68</sup>, I. Ferrero<sup>205</sup>, S. Ferriol<sup>51</sup>, P. Ferruit<sup>26</sup>, D. Filleul<sup>99</sup>, F. Finelli<sup>35,139</sup>, S. L. Finkelstein<sup>65</sup>, A. Finoguenov<sup>206</sup>, B. Fiorini<sup>63,207</sup>, F. Flentge<sup>170</sup>, P. Focardi<sup>72</sup>, J. Fonseca<sup>55,175</sup>, A. Fontana<sup>142</sup>, F. Fontanot<sup>59,58</sup>, F. Fornari<sup>139</sup>, P. Fosalba<sup>143,133</sup>, M. Fossati<sup>34,208</sup>, S. Fotopoulou<sup>130</sup>, D. Fouchez<sup>52</sup>, N. Fourmanoit<sup>52</sup>, M. Frailis<sup>59</sup>, D. Fraix-Burnet<sup>209</sup>, E. Franceschi<sup>35</sup>, A. Franco<sup>185,184,186</sup>, P. Franzetti<sup>108</sup>, J. Friehoefer<sup>170</sup>, C. S. Frenk<sup>87</sup>, G. Frittoli<sup>176</sup>, P.-A. Frugier<sup>11</sup>, N. Frusciante<sup>131</sup>, A. Fumagalli<sup>105,59,58</sup>, M. Fumagalli<sup>59,208</sup>, M. Fumana<sup>108</sup>, Y. Fu<sup>70,69</sup>, L. Gabarra<sup>171</sup>, S. Galeotta<sup>59</sup>, L. Galluccio<sup>8</sup>, K. Ganga<sup>10</sup>, H. Gao<sup>157</sup>, J. García-Bellido<sup>14</sup>, K. Garcia<sup>210</sup>, J. P. Gardner<sup>211</sup>, B. Garilli<sup>108</sup>, L.-M. Gaspar-Venancio<sup>104</sup>, T. Gasparetto<sup>59</sup>, V. Gautard<sup>212</sup>, R. Gavazzi<sup>20,2</sup>, E. Gaztanaga<sup>132,143,63</sup>, L. Genolet<sup>125</sup>, R. Genova Santos<sup>67,181</sup>, F. Gentile<sup>72,35</sup>, K. George<sup>82</sup>, M. Gerbino<sup>42</sup>, Z. Ghaffari<sup>59,58</sup>, F. Giacomini<sup>73</sup>, F. Gianotti<sup>35</sup>, G. P. S. Gibb<sup>98</sup>, W. Gillard<sup>52</sup>, B. Gillis<sup>98</sup>, M. Ginolfi<sup>213,172</sup>, C. Giocoli<sup>35,214</sup>, M. Girardi<sup>113,59</sup>, S. K. Giri<sup>7,215</sup>, L. W. K. Goh<sup>11</sup>, P. Gómez-Alvarez<sup>216,26</sup>, V. Gonzalez-Perez<sup>217</sup>, A. H. Gonzalez<sup>210</sup>, E. J. Gonzalez<sup>57,140,218</sup>, J. C. Gonzalez<sup>26,219</sup>, S. Gouyou Beauchamps<sup>143,133</sup>, G. Gozalias<sup>220,206</sup>, J. Gracia-Carpio<sup>93</sup>, S. Grandis<sup>173</sup>, B. R. Granett<sup>34</sup>, M. Granvik<sup>206,221</sup>, A. Grazian<sup>75</sup>, A. Gregorio<sup>113,59,60</sup>, C. Grenet<sup>2</sup>, C. Grillo<sup>43,108</sup>, F. Grupp<sup>93,82</sup>, C. Gruppioni<sup>35</sup>, A. Gruppuso<sup>35,73</sup>, C. Guerbuez<sup>170</sup>, S. Guerrini<sup>222</sup>, M. Guidi<sup>72,35</sup>, P. Guillard<sup>121,2</sup>, C. M. Gutierrez<sup>181</sup>, P. Guttridge<sup>16</sup>, L. Guzzo<sup>43,34</sup>, S. Gwyn<sup>223</sup>, J. Haapala<sup>224</sup>, J. Haase<sup>93</sup>, C. R. Haddow<sup>170</sup>, M. Hailey<sup>16</sup>, A. Hall<sup>98</sup>, D. Hall<sup>225</sup>, N. Hamaus<sup>82,226</sup>, B. S. Haridasu<sup>61,60,58</sup>, J. Harnois-Déraps<sup>47</sup>, C. Harper<sup>227</sup>, W. G. Hartley<sup>125</sup>, G. Hasinger<sup>228,229</sup>, F. Hassani<sup>205</sup>, N. A. Hatch<sup>56</sup>, S. V. H. Haugan<sup>205</sup>, B. Häußler<sup>230</sup>, A. Heavens<sup>162</sup>, L. Heisenberg<sup>31</sup>, A. Helmi<sup>69</sup>, G. Helou<sup>62</sup>, S. Hemmati<sup>62</sup>, K. Henares<sup>26</sup>, O. Herent<sup>2</sup>, C. Hernández-Monteagudo<sup>196,68,67</sup>, T. Heuberger<sup>231</sup>, P. C. Hewett<sup>232</sup>, S. Heydenreich<sup>138,233</sup>, H. Hildebrandt<sup>234</sup>, M. Hirschmann<sup>235,59</sup>, J. Hjorth<sup>236</sup>, J. Hoar<sup>26</sup>, H. Hoekstra<sup>70,\*\*\*</sup>, A. D. Holland<sup>225,201</sup>, M. S. Holliman<sup>98</sup>, W. Holmes<sup>112</sup>, I. Hook<sup>200</sup>, B. Horeau<sup>11</sup>, F. Hormuth<sup>237</sup>, A. Hornstrup<sup>238,147</sup>, S. Hosseini<sup>92</sup>, D. Hu<sup>16</sup>, P. Hudelot<sup>2</sup>, M. J. Hudson<sup>76,77,109</sup>, M. Huertas-Company<sup>67,181,239,240</sup>, E. M. Huff<sup>112</sup>, A. C. N. Hughes<sup>162</sup>, A. Humphrey<sup>55,241</sup>, L. K. Hunt<sup>172</sup>, D. D. Huynh<sup>212</sup>, R. Ibata<sup>97</sup>, K. Ichikawa<sup>242</sup>, S. Iglesias-Groth<sup>67</sup>, O. Ilbert<sup>20</sup>, S. Ilic<sup>243,92</sup>, L. Ingolia<sup>164</sup>, E. Iodice<sup>24</sup>, H. Israel<sup>244</sup>, U. E. Israelsson<sup>112</sup>, L. Izzo<sup>24</sup>, P. Jablonka<sup>4</sup>, N. Jackson<sup>122</sup>, J. Jacobson<sup>62</sup>, M. Jafariyazani<sup>62</sup>, K. Jahnke<sup>78</sup>, B. Jain<sup>245</sup>, H. Jansen<sup>173</sup>, M. J. Jarvis<sup>171</sup>, J. Jasche<sup>246,1</sup>, M. Jauzac<sup>247,87,248,249</sup>, N. Jeffrey<sup>204</sup>, M. Jhabvala<sup>250</sup>, Y. Jimenez-Teja<sup>27,195</sup>, A. Jimenez Muñoz<sup>19</sup>, B. Joachimi<sup>204</sup>, P. H. Johansson<sup>206</sup>, S. Joudaki<sup>63</sup>, E. Jullo<sup>20</sup>, J. J. E. Kajava<sup>251,252</sup>, Y. Kang<sup>125</sup>, A. Kannawadi<sup>253</sup>, V. Kansal<sup>254,255</sup>, D. Karagiannis<sup>207,256</sup>, M. Kärcher<sup>20,91</sup>, A. Kashlinsky<sup>211,257,258</sup>, M. V. Kazandjian<sup>70,259</sup>, F. Keck<sup>170</sup>, E. Keihänen<sup>224</sup>, E. Kerins<sup>122</sup>, S. Kermiche<sup>52</sup>, A. Khalil<sup>16</sup>, A. Kiessling<sup>112</sup>, K. Kiiveri<sup>224</sup>, M. Kilbinger<sup>11</sup>, J. Kim<sup>171</sup>, R. King<sup>227</sup>, C. C. Kirkpatrick<sup>224</sup>, T. Kitching<sup>16</sup>, M. Kluge<sup>93</sup>, M. Knabenhans<sup>7</sup>, J. H. Knapen<sup>67,68</sup>, A. Knebe<sup>217,260,261</sup>, J.-P. Kneib<sup>4</sup>, R. Kohley<sup>26</sup>, L. V. E. Koopmans<sup>69</sup>, H. Koskinen<sup>206</sup>, E. Koulouridis<sup>11,262</sup>, R. Kou<sup>10,263</sup>, A. Kovács<sup>264,265</sup>, I. Kovačić<sup>64</sup>, A. Kowalczyk<sup>170</sup>, K. Koyama<sup>63</sup>, K. Kraljic<sup>97</sup>, O. Krause<sup>78</sup>, S. Kruk<sup>26</sup>, B. Kubik<sup>51</sup>, U. Kuchner<sup>266</sup>,

K. Kuijken<sup>70</sup>, M. Kümmel<sup>82</sup>, M. Kunz<sup>111</sup>, H. Kurki-Suonio<sup>206,267</sup>, F. Lacasa<sup>163,9,111</sup>, C. G. Lacey<sup>87</sup>,  
 F. La Franca<sup>182</sup>, N. Lagarde<sup>120</sup>, O. Lahav<sup>204</sup>, C. Laigle<sup>2</sup>, A. La Marca<sup>268,69</sup>, O. La Marle<sup>83</sup>, B. Lamine<sup>92</sup>,  
 M. C. Lam<sup>98</sup>, A. Lançon<sup>97</sup>, H. Landt<sup>247</sup>, M. Langer<sup>9</sup>, A. Lapi<sup>61,58,101,60</sup>, C. Larcheveque<sup>269</sup>, S. S. Larsen<sup>270</sup>,  
 M. Lattanzi<sup>42</sup>, F. Laudisio<sup>39</sup>, D. Laugier<sup>52</sup>, R. Laureijs<sup>104</sup>, V. Laurent<sup>9</sup>, G. Lavaux<sup>2</sup>, A. Lawrenson<sup>271,16</sup>,  
 A. Lazanu<sup>122</sup>, T. Lazeyras<sup>208</sup>, Q. Le Boulc'h<sup>272</sup>, A. M. C. Le Brun<sup>41,2</sup>, V. Le Brun<sup>20</sup>, F. Leclercq<sup>2</sup>, S. Lee<sup>112</sup>,  
 J. Le Graet<sup>52</sup>, L. Legrand<sup>273</sup>, K. N. Leirvik<sup>205</sup>, M. Le Jeune<sup>10</sup>, M. Lembo<sup>29,42</sup>, D. Le Mignant<sup>20</sup>,  
 M. D. Lepinzan<sup>113,59</sup>, F. Lepori<sup>7</sup>, A. Le Reun<sup>1</sup>, G. Leroy<sup>247,87</sup>, G. F. Lesci<sup>164,35</sup>, J. Lesgourgues<sup>154</sup>,  
 L. Leuzzi<sup>164,35</sup>, M. E. Levi<sup>274</sup>, T. I. Liaudat<sup>45</sup>, G. Libet<sup>83</sup>, P. Liebing<sup>16</sup>, S. Ligorì<sup>110</sup>, P. B. Lilje<sup>205</sup>, C.-C. Lin<sup>157</sup>,  
 D. Linde<sup>180</sup>, E. Linder<sup>275</sup>, V. Lindholm<sup>206,267</sup>, L. Linke<sup>173</sup>, S.-S. Li<sup>70</sup>, S. J. Liu<sup>194</sup>, I. Lloro<sup>276</sup>,  
 F. S. N. Lobo<sup>153,18</sup>, N. Lodieu<sup>67,181</sup>, M. Lombardi<sup>43</sup>, L. Lombriser<sup>111</sup>, P. Lonare<sup>176,145</sup>, G. Longo<sup>131,117</sup>,  
 M. López-Caniego<sup>277,278</sup>, X. Lopez Lopez<sup>72,279</sup>, J. Lorenzo Alvarez<sup>104</sup>, A. Loureiro<sup>280,162</sup>, J. Loveday<sup>263</sup>,  
 E. Lusso<sup>172,213</sup>, J. Macias-Perez<sup>19</sup>, T. Maciaszek<sup>83</sup>, G. Maggio<sup>59</sup>, M. Magliocchetti<sup>194</sup>, F. Magnard<sup>2</sup>,  
 E. A. Magnier<sup>157</sup>, A. Magro<sup>281</sup>, G. Mahler<sup>282,247,87</sup>, G. Mainetti<sup>272</sup>, D. Maino<sup>43,108,44</sup>,  
 E. Maiorano<sup>35</sup>, E. Maiorano<sup>104</sup>, N. Malavasi<sup>93</sup>, G. A. Mamon<sup>2,1</sup>, C. Mancini<sup>108</sup>, R. Mandelbaum<sup>283</sup>,  
 M. Manera<sup>57,284</sup>, A. Manjón-García<sup>192</sup>, F. Mannucci<sup>172</sup>, O. Mansutti<sup>59</sup>, M. Manteiga Outeiro<sup>177</sup>,  
 R. Maoli<sup>187,142</sup>, C. Maraston<sup>63</sup>, S. Marcin<sup>231</sup>, P. Marcos-Arenal<sup>285</sup>, B. Margalef-Bentabol<sup>268</sup>, O. Marggraf<sup>138</sup>,  
 D. Marinucci<sup>176</sup>, M. Marinucci<sup>189,40,39</sup>, K. Markovic<sup>112</sup>, F. R. Marleau<sup>173</sup>, J. Marpaud<sup>19</sup>, J. Martignac<sup>11</sup>,  
 J. Martín-Fleitas<sup>277</sup>, P. Martin-Moruno<sup>48</sup>, E. L. Martin<sup>181</sup>, M. Martinelli<sup>142,148</sup>, N. Martinet<sup>20</sup>, H. Martin<sup>77,76</sup>,  
 C. J. A. P. Martins<sup>191,55</sup>, F. Marulli<sup>164,35,73</sup>, D. Massari<sup>35</sup>, R. Massey<sup>247,87</sup>, D. C. Masters<sup>17</sup>,  
 S. Matarrese<sup>40,75,39,286</sup>, Y. Matsuoka<sup>287</sup>, S. Matthew<sup>98</sup>, B. J. Maughan<sup>130</sup>, N. Mauri<sup>159,73</sup>, L. Maurin<sup>9</sup>,  
 S. Maurogordato<sup>8</sup>, K. McCarthy<sup>112</sup>, A. W. McConnachie<sup>223</sup>, H. J. McCracken<sup>2</sup>, I. McDonald<sup>122</sup>,  
 J. D. McEwen<sup>16</sup>, C. J. R. McPartland<sup>147,288</sup>, E. Medinaceli<sup>35</sup>, V. Mehta<sup>62</sup>, S. Mei<sup>10</sup>, M. Melchior<sup>231</sup>,  
 J.-B. Melin<sup>289</sup>, B. Ménard<sup>3</sup>, J. Mendes<sup>170</sup>, J. Mendez-Abreu<sup>68,67</sup>, M. Meneghetti<sup>35,73</sup>, A. Mercurio<sup>24,123,124</sup>,  
 E. Merlin<sup>142</sup>, R. B. Metcalf<sup>164,35</sup>, G. Meylan<sup>4</sup>, M. Migliaccio<sup>176,94</sup>, M. Mignoli<sup>35</sup>, L. Miller<sup>171</sup>, M. Miluzio<sup>26,285</sup>,  
 B. Milvang-Jensen<sup>147,288</sup>, J. P. Mimoso<sup>153,18</sup>, R. Miquel<sup>57,290</sup>, H. Miyatake<sup>291,292,103</sup>, B. Mobasher<sup>293</sup>,  
 J. J. Mohr<sup>82,93</sup>, P. Monaco<sup>113,59,60,58</sup>, M. Monguió<sup>150,294</sup>, A. Montoro<sup>132,143</sup>, A. Mora<sup>277</sup>,  
 A. Moradinezhad Dizgah<sup>295,111</sup>, M. Moresco<sup>164,35</sup>, C. Moretti<sup>61,156,59,58,60</sup>, G. Morgante<sup>35</sup>, N. Morisset<sup>125</sup>,  
 T. J. Moriya<sup>296,297</sup>, P. W. Morris<sup>197</sup>, D. J. Mortlock<sup>162,298,246</sup>, L. Moscardini<sup>164,35,73</sup>, D. F. Mota<sup>205</sup>, S. Mottet<sup>2</sup>,  
 L. A. Moustakas<sup>112</sup>, T. Moutard<sup>26</sup>, T. Müller<sup>93</sup>, E. Munari<sup>59,58</sup>, G. Murphree<sup>157</sup>, C. Murray<sup>10</sup>, N. Murray<sup>225</sup>,  
 P. Musi<sup>38</sup>, S. Nadathur<sup>63</sup>, B. C. Nagam<sup>69</sup>, T. Nagao<sup>287</sup>, K. Naidoo<sup>204</sup>, R. Nakajima<sup>138</sup>, C. Nally<sup>98</sup>, P. Natoli<sup>29,42</sup>,  
 A. Navarro-Alsina<sup>138</sup>, D. Navarro Girones<sup>132,143</sup>, C. Neissner<sup>57,140</sup>, A. Nersesian<sup>282,64</sup>, S. Nesseris<sup>14</sup>,  
 H. N. Nguyen-Kim<sup>2</sup>, L. Nicastro<sup>35</sup>, R. C. Nichol<sup>30</sup>, M. Nielbock<sup>78</sup>, S.-M. Niemi<sup>104</sup>, S. Nieto<sup>26</sup>, K. Nilsson<sup>299</sup>,  
 J. Noller<sup>204,63</sup>, P. Norberg<sup>247,87</sup>, A. Nouri-Zonoz<sup>111</sup>, P. Ntelis<sup>52</sup>, A. A. Nucita<sup>184,185,186</sup>, P. Nugent<sup>274</sup>,  
 N. J. Nunes<sup>153,18</sup>, T. Nutma<sup>69,70</sup>, I. Ocampo<sup>14</sup>, J. Odier<sup>19</sup>, P. A. Oesch<sup>125,288,147</sup>, M. Oguri<sup>300,301</sup>,  
 D. Magalhaes Oliveira<sup>18,153</sup>, M. Onoue<sup>103</sup>, T. Oosterbroek<sup>104</sup>, F. Oppizzi<sup>39,40</sup>, C. Ordenovic<sup>8</sup>, K. Osato<sup>300,103</sup>,  
 F. Pacaud<sup>138</sup>, F. Pace<sup>144,13,110</sup>, C. Padilla<sup>57</sup>, K. Paech<sup>93</sup>, L. Pagano<sup>29,42</sup>, M. J. Page<sup>16</sup>, E. Palazzi<sup>35</sup>,  
 S. Paltani<sup>125</sup>, S. Pamuk<sup>154</sup>, S. Pandolfi<sup>104</sup>, D. Paoletti<sup>35,139</sup>, M. Paolillo<sup>302,24,117</sup>, P. Papaderos<sup>55</sup>,  
 K. Pardede<sup>180</sup>, G. Paribelli<sup>132,303,61</sup>, A. Parmar<sup>162</sup>, C. Partmann<sup>32</sup>, F. Pasian<sup>59</sup>, F. Passalacqua<sup>40,39</sup>,  
 K. Paterson<sup>78</sup>, L. Patrizii<sup>73</sup>, C. Pattison<sup>63</sup>, A. Paulino-Afonso<sup>191,55</sup>, R. Paviot<sup>11</sup>, J. A. Peacock<sup>98</sup>, F. R. Pearce<sup>56</sup>,  
 K. Pedersen<sup>304</sup>, A. Peel<sup>4</sup>, R. F. Peletier<sup>69</sup>, M. Pellejero Ibanez<sup>98,36</sup>, R. Pello<sup>20</sup>, M. T. Penny<sup>305</sup>,  
 W. J. Percival<sup>77,76,109</sup>, A. Perez-Garrido<sup>192</sup>, L. Perotto<sup>19</sup>, V. Pettorino<sup>104</sup>, A. Pezzotta<sup>93</sup>, S. Pezzuto<sup>194</sup>,  
 A. Philippon<sup>9</sup>, M. Pierre<sup>11</sup>, O. Piersanti<sup>104</sup>, M. Pietroni<sup>179,180</sup>, L. Piga<sup>179,180,108</sup>, L. Pilo<sup>306</sup>, S. Pires<sup>11</sup>,  
 A. Pisani<sup>52,307,203,308</sup>, A. Pizzella<sup>40,75</sup>, L. Pizzuti<sup>208</sup>, C. Plana<sup>16</sup>, G. Polenta<sup>107</sup>, J. E. Pollack<sup>212,10</sup>, M. Poncet<sup>83</sup>,  
 M. Pöntinen<sup>206</sup>, P. Pool<sup>309</sup>, L. A. Popa<sup>310</sup>, V. Popa<sup>310</sup>, J. Popp<sup>199</sup>, C. Porciani<sup>138</sup>, L. Porth<sup>138</sup>, D. Potter<sup>7</sup>,  
 M. Poulain<sup>311</sup>, A. Pourtsidou<sup>98,312</sup>, L. Pozzetti<sup>35</sup>, I. Prandoni<sup>101</sup>, G. W. Pratt<sup>11</sup>, S. Prezelus<sup>104</sup>, E. Prieto<sup>20</sup>,  
 A. Pugno<sup>138</sup>, S. Quai<sup>164,35</sup>, L. Quilley<sup>313</sup>, G. D. Racca<sup>104</sup>, A. Raccanelli<sup>40,39,75,314</sup>, G. Rácz<sup>112</sup>,  
 S. Radinović<sup>132,205</sup>, M. Radovich<sup>75</sup>, A. Ragagnin<sup>35,58,164,156</sup>, U. Ragnit<sup>104</sup>, F. Raison<sup>93</sup>,  
 N. Ramos-Chernenko<sup>67,181</sup>, C. Ranc<sup>2</sup>, Y. Raser<sup>41,121</sup>, N. Rayle<sup>99</sup>, R. Rebolo<sup>67,68</sup>, A. Refregier<sup>12</sup>, P. Reimberg<sup>1</sup>,  
 T. H. Reiprich<sup>138</sup>, F. Renk<sup>170</sup>, A. Renzi<sup>40,39</sup>, J. Retre<sup>137</sup>, Y. Revaz<sup>4</sup>, C. Reylé<sup>315</sup>, L. Reynolds<sup>57</sup>,  
 J. Rhodes<sup>112</sup>, F. Ricci<sup>182,142</sup>, M. Ricci<sup>8,10</sup>, G. Riccio<sup>24</sup>, S. O. Ricken<sup>170</sup>, S. Rissanen<sup>206</sup>, I. Risso<sup>303</sup>,  
 H.-W. Rix<sup>78</sup>, A. C. Robin<sup>315</sup>, B. Rocca-Volmerange<sup>1,2</sup>, P.-F. Rocci<sup>9</sup>, M. Rodenhuis<sup>316</sup>, G. Rodighiero<sup>40,75</sup>,  
 M. Rodriguez Monroy<sup>14</sup>, R. P. Rollins<sup>98</sup>, M. Romanello<sup>72,35</sup>, J. Roman<sup>68,67</sup>, E. Romelli<sup>59</sup>,  
 M. Romero-Gomez<sup>150,143,151</sup>, M. Roncarelli<sup>35</sup>, P. Rosati<sup>29,35</sup>, C. Rosset<sup>10</sup>, E. Rossetti<sup>72</sup>, W. Roster<sup>93,234</sup>,

H. J. A. Rottgering<sup>70</sup>, A. Rozas-Fernández<sup>18</sup>, K. Ruane<sup>16</sup>, J. A. Rubino-Martin<sup>67,68</sup>, A. Rudolph<sup>170</sup>, F. Ruppin<sup>51</sup>, B. Rusholme<sup>62</sup>, S. Sacquegnà<sup>184,185,186</sup>, I. Sáez-Casares<sup>41</sup>, S. Saga<sup>291</sup>, R. Saglia<sup>82,93</sup>, M. Sahlén<sup>317</sup>, T. Saifollahi<sup>97,69</sup>, Z. Sakr<sup>31,92,318</sup>, J. Salvalaggio<sup>113,59,58,60</sup>, R. Salvaterra<sup>108</sup>, L. Salvati<sup>9</sup>, M. Salvato<sup>93</sup>, J.-C. Salvignol<sup>104</sup>, A. G. Sánchez<sup>93</sup>, E. Sanchez<sup>152</sup>, D. B. Sanders<sup>157</sup>, D. Sapone<sup>319</sup>, M. Saponara<sup>38</sup>, E. Sarpa<sup>61,156,60</sup>, F. Sarron<sup>320,92</sup>, S. Sartori<sup>52</sup>, B. Sartoris<sup>82,59</sup>, B. Sassolas<sup>51</sup>, L. Sauniere<sup>52</sup>, M. Sauvage<sup>11</sup>, M. Sawicki<sup>190</sup>, R. Scaramella<sup>142,148</sup>, C. Scarlata<sup>135</sup>, L. Scharre<sup>235</sup>, J. Schaye<sup>70</sup>, J. A. Schewtschenko<sup>98</sup>, J.-T. Schindler<sup>321</sup>, E. Schinnerer<sup>78</sup>, M. Schirmer<sup>78</sup>, F. Schmidt<sup>32,226</sup>, F. Schmidt<sup>170</sup>, M. Schmidt<sup>170</sup>, A. Schneider<sup>7</sup>, M. Schneider<sup>170</sup>, P. Schneider<sup>138</sup>, N. Schöneberg<sup>150</sup>, T. Schrabback<sup>173</sup>, M. Schultheis<sup>8</sup>, S. Schulz<sup>7</sup>, N. Schuster<sup>82</sup>, J. Schwartz<sup>170</sup>, D. Sciotti<sup>142,148</sup>, M. Scodeggio<sup>108</sup>, D. Scognamiglio<sup>112</sup>, D. Scott<sup>322</sup>, V. Scottez<sup>1,323</sup>, A. Secroun<sup>52</sup>, E. Sefusatti<sup>59,58,60</sup>, G. Seidel<sup>78</sup>, M. Seiffert<sup>112</sup>, E. Sellentin<sup>324,70</sup>, M. Selwood<sup>130</sup>, E. Semboloni<sup>5</sup>, M. Sereno<sup>35,73</sup>, S. Serjeant<sup>199</sup>, S. Serrano<sup>143,325,132</sup>, G. Setnikar<sup>51</sup>, F. Shankar<sup>326</sup>, R. M. Sharples<sup>247</sup>, A. Short<sup>104</sup>, A. Shulevski<sup>327,69,328</sup>, M. Shuntov<sup>1,147,288</sup>, M. Sias<sup>38</sup>, G. Sikkema<sup>69</sup>, A. Silvestri<sup>5</sup>, P. Simon<sup>138</sup>, C. Sirignano<sup>40,39</sup>, G. Sirri<sup>73</sup>, J. Skottfelt<sup>225</sup>, E. Slezak<sup>8</sup>, D. Sluse<sup>282</sup>, G. P. Smith<sup>329</sup>, L. C. Smith<sup>232</sup>, R. E. Smith<sup>263</sup>, S. J. A. Smit<sup>16</sup>, F. Soldano<sup>2</sup>, B. G. B. Solheim<sup>330</sup>, J. G. Sorce<sup>331,9,160</sup>, F. Sorrenti<sup>111</sup>, E. Soubrie<sup>9</sup>, L. Spinoglio<sup>194</sup>, A. Spurio Mancini<sup>332,16</sup>, J. Stadel<sup>7</sup>, L. Stagnaro<sup>104</sup>, L. Stanco<sup>39</sup>, S. A. Stanford<sup>333</sup>, J.-L. Starck<sup>11</sup>, P. Stassi<sup>19</sup>, J. Steinwagner<sup>93</sup>, D. Stern<sup>112</sup>, C. Stone<sup>334</sup>, P. Strada<sup>104</sup>, F. Strafella<sup>184,186,185</sup>, D. Stramaccioni<sup>104</sup>, C. Surace<sup>20</sup>, F. Sureau<sup>11</sup>, S. H. Suyu<sup>33,32,335</sup>, I. Swindells<sup>309</sup>, M. Szafraniec<sup>104</sup>, I. Szapudi<sup>157</sup>, S. Taamoli<sup>293</sup>, M. Talia<sup>164,35</sup>, P. Tallada-Crespi<sup>152,140</sup>, K. Tanidis<sup>171</sup>, C. Tao<sup>52</sup>, P. Tarrío<sup>336,11</sup>, D. Tavagnacco<sup>59</sup>, A. N. Taylor<sup>98</sup>, J. E. Taylor<sup>76,77</sup>, P. L. Taylor<sup>337,338</sup>, E. M. Teixeira<sup>339</sup>, M. Tenti<sup>73</sup>, P. Teodoro Idiago<sup>277</sup>, H. I. Teplitz<sup>17</sup>, I. Tereno<sup>153,137</sup>, N. Tessore<sup>204</sup>, V. Testa<sup>142</sup>, G. Testera<sup>127</sup>, M. Tewes<sup>138</sup>, R. Teyssier<sup>307</sup>, N. Theret<sup>83</sup>, C. Thizy<sup>340</sup>, P. D. Thomas<sup>16</sup>, Y. Toba<sup>341</sup>, S. Toft<sup>147,288</sup>, R. Toledo-Moreo<sup>342</sup>, E. Tolstoy<sup>69</sup>, E. Tommasi<sup>343</sup>, O. Torbaniuk<sup>164</sup>, F. Torradeflot<sup>140,152</sup>, C. Tortora<sup>24</sup>, S. Tosi<sup>126,127</sup>, S. Tosti<sup>9</sup>, M. Trifoglio<sup>35</sup>, A. Troja<sup>40,39</sup>, T. Trombetti<sup>101</sup>, A. Tronconi<sup>73,159</sup>, M. Tsedrik<sup>98</sup>, A. Tsyganov<sup>198</sup>, M. Tucci<sup>125</sup>, I. Tutusaus<sup>92</sup>, C. Uhlemann<sup>155,47</sup>, L. Ulivi<sup>344,213,172</sup>, M. Urbano<sup>97</sup>, L. Vacher<sup>61</sup>, L. Vaillon<sup>99</sup>, P. Valageas<sup>95</sup>, I. Valdes<sup>157</sup>, E. A. Valentijn<sup>69</sup>, L. Valenziano<sup>35,139</sup>, C. Valieri<sup>73</sup>, J. Valiviita<sup>206,267</sup>, M. Van den Broeck<sup>170,345</sup>, T. Vassallo<sup>82,59</sup>, R. Vavrek<sup>26</sup>, J. Vega-Ferrero<sup>196,136</sup>, B. Venemans<sup>70</sup>, A. Venhola<sup>311</sup>, S. Ventura<sup>39</sup>, G. Verdoes Kleijn<sup>69</sup>, D. Vergani<sup>35</sup>, A. Verma<sup>171</sup>, F. Vernizzi<sup>95</sup>, A. Veropalumbo<sup>34,127,303</sup>, G. Verza<sup>346,203</sup>, C. Vescovi<sup>19</sup>, D. Vibert<sup>20</sup>, M. Viel<sup>58,59,61,60,156</sup>, P. Vielzeuf<sup>52</sup>, C. Viglione<sup>143,132</sup>, A. Viitanen<sup>224,142</sup>, F. Villaescusa-Navarro<sup>203,307</sup>, S. Vinciguerra<sup>20</sup>, F. Visticot<sup>11</sup>, K. Voggel<sup>97</sup>, M. von Wietersheim-Kramsta<sup>87,247,204</sup>, W. J. Vriend<sup>69</sup>, S. Wachter<sup>158</sup>, M. Walmsley<sup>149,122</sup>, G. Walth<sup>62</sup>, D. M. Walton<sup>16</sup>, N. A. Walton<sup>232</sup>, M. Wander<sup>225</sup>, L. Wang<sup>268,69</sup>, Y. Wang<sup>17</sup>, J. R. Weaver<sup>86</sup>, J. Weller<sup>82,93</sup>, M. Wetzstein<sup>93</sup>, D. J. Whalen<sup>63</sup>, I. H. Whittam<sup>171,256</sup>, A. Widmer<sup>10</sup>, M. Wiesmann<sup>205</sup>, J. Wilde<sup>199</sup>, O. R. Williams<sup>198</sup>, H.-A. Winther<sup>205</sup>, A. Wittje<sup>234</sup>, J. H. W. Wong<sup>122</sup>, A. H. Wright<sup>234</sup>, V. Yankelevich<sup>347</sup>, H. W. Yeung<sup>98</sup>, M. Yoon<sup>70</sup>, S. Youles<sup>63</sup>, L. Y. A. Yung<sup>250,348</sup>, A. Zacchei<sup>59,58</sup>, L. Zalesky<sup>157</sup>, G. Zamorani<sup>35</sup>, A. Zamorano Vitorelli<sup>112</sup>, M. Zannoni Marc<sup>99</sup>, M. Zennaro<sup>171</sup>, F. M. Zerbi<sup>34</sup>, I. A. Zinchenko<sup>82</sup>, J. Zoubian<sup>52</sup>, E. Zucca<sup>35</sup>, and M. Zumalacarregui<sup>128</sup>

(Affiliations can be found after the references)

Received 21 May 2024 / Accepted 28 August 2024

## ABSTRACT

The current standard model of cosmology successfully describes a variety of measurements, but the nature of its main ingredients, dark matter and dark energy, remains unknown. *Euclid* is a medium-class mission in the Cosmic Vision 2015–2025 programme of the European Space Agency (ESA) that will provide high-resolution optical imaging, as well as near-infrared imaging and spectroscopy, over about 14 000 deg<sup>2</sup> of extragalactic sky. In addition to accurate weak lensing and clustering measurements that probe structure formation over half of the age of the Universe, its primary probes for cosmology, these exquisite data will enable a wide range of science. This paper provides a high-level overview of the mission, summarising the survey characteristics, the various data-processing steps, and data products. We also highlight the main science objectives and expected performance.

**Key words.** instrumentation: detectors – instrumentation: spectrographs – space vehicles: instruments – telescopes – surveys – cosmology: observations

## 1. Introduction

A century of ever improving observations has resulted in a concordance cosmological model that is surprisingly simple: only six numbers are currently needed to describe a wide variety

of precise measurements (Planck Collaboration VI 2020). The result, however, is also unsatisfactory because it highlights a serious problem for our understanding of fundamental physics and astronomy: it relies on assumptions about the initial conditions and the theory of gravity, while the nature of the main

ingredients, dark matter and dark energy, remain great mysteries. The observational evidence for a largely ‘dark’ universe is overwhelming, demonstrating that our theories of particle physics and/or gravity are either incomplete or incorrect. Moreover, we lack compelling theoretical guidance to solve this crisis in fundamental physics (Albrecht et al. 2006; Amendola et al. 2018).

Arguably, the biggest challenge is the observation that the expansion of the Universe is accelerating (e.g. Riess et al. 1998; Perlmutter et al. 1999; Eisenstein et al. 2005; Betoule et al. 2014). Current explanations range from Einstein’s cosmological constant, dynamic mechanisms such as quintessence, or a modification of the laws of gravity on cosmological scales (see Amendola et al. 2018, for an extensive overview of ideas). To robustly distinguish between these different theoretical ideas, the precision of the measurements needs to improve by at least an order of magnitude, whilst our ability to interpret the data correctly has to advance accordingly if we are to take advantage of the smaller statistical uncertainties.

The exquisite observations of the temperature fluctuations in the cosmic microwave background (CMB) performed by WMAP (Hinshaw et al. 2013) and *Planck* (Planck Collaboration I 2020) have been crucial to establish the baseline cosmological constant-dominated cold dark matter ( $\Lambda$ CDM) model. This is because the physical interpretation of the measurements is relatively straightforward, and all-sky experiments from space benefit from a stable environment and superior control of instrumental effects. Unfortunately, the CMB provides limited information about the nature of dark matter and dark energy, because it primarily probes the physical conditions at the time of recombination, when dark energy was negligible. To quantify how the balance between dark matter and dark energy evolved, the CMB results need to be complemented by high-quality measurements of the cosmic expansion history and the growth of large-scale structure (LSS) over the past eight billion years or more. In principle, such studies can provide complementary constraints on the initial conditions, explore modifications of the theory of general relativity on cosmological scales, and determine the neutrino mass scale (Albrecht et al. 2006). Research in observational cosmology is therefore shifting towards studies of the LSS, and a number of large spectroscopic and imaging surveys will collect vast amounts of data in the coming decade. For instance, the Legacy Survey of Space and Time (LSST) by the Vera C. Rubin Observatory will repeatedly image the entire southern sky in multiple bands (Ivezić et al. 2019), while the Dark Energy Spectroscopic Instrument experiment (DESI) will measure redshifts for about 40 million galaxies (DESI Collaboration 2024). These projects are major improvements over previous surveys, but a robust interpretation is essential. Accounting for the complexities of ground-based data, in particular the variable sky conditions, presents a major challenge. Hence, further advances will come from space-based facilities, such as *Euclid* (Laureijs et al. 2011) and the planned *Nancy Grace Roman* Space Telescope (Akeson et al. 2019).

This paper describes the background, instruments, performance, and planned science of *Euclid*, a medium-class mission in the Cosmic Vision 2015–2025 programme of the European Space Agency (ESA). *Euclid* resulted from a 2007 call by ESA for the selection of a medium-sized space mission. Besides five other mission proposals, a dark energy mission concept was included for competitive down-selection. This new mission concept, ultimately named *Euclid*, was based on a combination of two initial dark-energy mission proposals, the Dark Universe Explorer (DUNE; Refregier 2009) and the Spectroscopic

All-Sky Cosmic Explorer (SPACE; Cimatti et al. 2009). It envisioned an extragalactic sky survey with visual imaging, and near-infrared photometry and spectroscopy, optimised for the measurement of the two primary cosmology probes, namely galaxy clustering and weak gravitational lensing, which are both powerful ways of measuring the evolution of the LSS, whilst complementing each other in terms of constraining power.

The main science case of *Euclid* was presented in Laureijs et al. (2011), which formed the basis for the official selection of the concept by ESA in 2011, and adoption as a mission in 2012. Since then, the mission hardware and software have been built, culminating in the successful launch of *Euclid* on 1st July 2023 on a Falcon-9 rocket from Cape Canaveral. Here we provide an up-to-date high-level overview of the mission during its initial time in orbit, describing the survey, the data products, and the science that the Euclid Consortium aims to perform.

The structure of this paper is as follows. In Sect. 2 we summarise the main science objectives of the *Euclid* mission and introduce the primary cosmological probes that drove the design. In Sect. 3 we provide a brief overview of the spacecraft and its instruments. The survey characteristics and supporting observations are described in Sect. 4, while early results from the commissioning and performance verification are presented in Sect. 5. The main data products that will be released publicly comprise simulated data (Sect. 6) and the actual data processed through the *Euclid* Science Ground Segment (SGS) pipeline (Sect. 7). The cosmological inferences enabled by *Euclid* are discussed in Sect. 8. Additional cosmological probes that are enabled or enhanced by the *Euclid* data are reviewed in Sect. 9. Finally, the impact of *Euclid* is not limited to cosmology, and a taste of the wide range of astrophysics that will be done is presented in more detail in Sect. 10. To aid in the readability of this and accompanying papers, we include a glossary of acronyms in Appendix A. Unless specified otherwise, magnitudes and surface brightness values are reported using the AB magnitude system.

## 2. Primary probes for cosmology with *Euclid*

The biggest mysteries in cosmology are the nature of dark matter and dark energy. Indirect evidence for the existence of dark matter has come from a wide range of astronomical and cosmological observations, but if it is composed of new elementary particles outside the standard model of particle physics, direct detections in terrestrial experiments (e.g. Battaglieri et al. 2017) are likely to play a prominent role in establishing its nature. The situation is markedly different for the observed accelerating expansion of the Universe, where progress will most likely come from advances in observational cosmology. To explain the observations, a component with a negative equation-of-state parameter<sup>1</sup> is required, which is commonly referred to as dark energy. It makes up about 69% of the present-day energy density (Planck Collaboration VI 2020), but we do not know if it is a cosmological constant, a field that evolves dynamically, or reflects a more profound modification of the gravitation laws at cosmological scales (see e.g. Amendola et al. 2018). One of the key observables to distinguish between such models is the way the equation-of-state parameter  $w(z)$  varies with redshift. To allow for a convenient comparison between cosmological probes, we

<sup>1</sup> The equation-of-state parameter  $w$  relates the pressure  $P$  and the energy density  $\rho c^2$  of a substance as  $P \equiv w\rho c^2$ . In the case of a cosmological constant  $\Lambda \neq 0$ , or a non-zero vacuum energy density,  $w = -1$ , and the time derivative is zero.

adopt

$$w(z) = w_0 + w_a \frac{z}{1+z}, \quad (1)$$

which captures the dynamical nature of dark energy to first order in  $(1-a)$ , where  $a = 1/(1+z)$  is the scale factor. Here,  $w_0$  is the present day equation of state, and  $w_a$  quantifies the dependence with redshift. This extension corresponds to a basic non-clustering dynamical dark energy model, and constraints on the parameters  $w_0$  and  $w_a$  show how well *Euclid* can test this scenario. For completeness, we note that the cosmological constant corresponds to the choice  $w_0 = -1$  and  $w_a = 0$ .

We can quantify the performance of a particular survey by comparing the dark energy figure of merit (FoM), which we defined as the inverse square root of the covariance matrix determinant for the dark energy parameters (Wang 2008b),

$$\text{FoM} = \frac{1}{\sqrt{\det \text{Cov}(w_0, w_a)}}, \quad (2)$$

so that a larger value implies a more precise measurement of the dark energy properties<sup>2</sup>. The challenge for the experimental design, however, is to establish a minimum value to achieve. Laureijs et al. (2011) presented a statistical argument, concluding that the value of  $w$  needs to be determined with a precision of about 1% to robustly test the  $\Lambda$ CDM model. Specifically, one of the main objectives of *Euclid* is to constrain the dark energy equation of state so that  $\text{FoM} > 400$  for this baseline scenario.

This is a challenging target for two reasons. First, to achieve such statistical constraining power requires surveying a considerable fraction of the cosmological volume out to  $z = 2$  (see e.g. Amara & Réfrégier 2007), thus covering the epoch during which dark energy became the dominant component in the Universe. In the case of *Euclid*, the aim is to observe 14 000 deg<sup>2</sup> of extragalactic sky with low zodiacal background and low Galactic extinction (see Sect. 4 for details). Second, systematic biases need to be sufficiently small as to not overwhelm the orders of magnitude improvement in precision. The observational signatures of dark energy are subtle, and unrecognised instrumental effects could be mistaken for new physics. To minimise this, exquisite experimental control is paramount. Although still challenging (and dependent on the specific probe used), this is best achieved from space.

A measurement of the expansion history via the distance-redshift relation provides the most direct constraints on the equation of state of dark energy. More generally, it provides constraints on the relative balance of ingredients and spatial curvature via the Friedmann equations, which link the time evolution of the scale factor  $a(t)$  to these ingredients. The rate at which density fluctuations grow also depends on the background cosmology. Hence, studying the growth of LSS provides another way to infer information about the composition of the Universe. It has the added benefit that it can constrain additional cosmological parameters and provide some key tests of the underlying theory of gravity (Amendola et al. 2018).

The expansion history and growth of LSS can be probed using a variety of techniques, each with their own advantages and limitations. Clearly, to achieve  $\text{FoM} > 400$ , the probes of interest should depend on the properties of the dark energy. Although

some are more sensitive than others, no individual probe can reach the target FoM, given the practical constraints on the mission design (see Sect. 3). Instead, probes need to be combined. Ideally, the individual probes should have comparable sensitivity, but also complement each other in terms of observational needs and precision. That is, the sum should be more than its parts.

Analogous to the use of the dark energy equation of state, the dimensionless linear growth rate  $f_g(z)$  depends on  $\Omega_m(z)$ , the redshift-dependent ratio of matter density divided by the critical density,

$$f_g(z) \equiv \frac{d \ln g_+(z)}{d \ln a} \simeq [\Omega_m(z)]^{\gamma_g}, \quad (3)$$

where  $g_+(z)$  is the linear growth factor that relates the amplitude of a linear density fluctuation,  $\delta(\mathbf{x}, z)$ , to its present value via  $\delta(\mathbf{x}, z) = g_+(z) \delta(\mathbf{x}, 0)$ . As general relativity (GR) predicts a value of  $\gamma_g \simeq 0.55$  for a flat  $\Lambda$ CDM cosmology (e.g. Peebles 1980; Lahav et al. 1991), a measurement of  $f_g(z)$  can be used to constrain the composition of the Universe, similar to what is done for the expansion history. However, a detailed measurement of the growth rate as a function of redshift and possibly of scale, can also shed light on the nature of dark energy and the underlying theory of gravity. In fact, a dynamical, clustering dark energy component, as well as modifications of GR, would not only lead to a different  $\Omega_m(z)$  but also to  $\gamma_g \neq 0.55$  (Linder 2005). Therefore, another key objective of *Euclid* is to determine the value of  $\gamma_g$  with a precision better than 0.02 (68% confidence), sufficient to distinguish between GR and a wide range of modified gravity theories (Laureijs et al. 2011). Moreover, modified gravity theories tend to affect dynamical and relativistic observables differently (e.g. Amendola et al. 2018), suggesting that one would like to combine such probes.

These considerations, combined with specific mission constraints, led to the decision to optimise *Euclid* for two powerful and highly complementary probes, namely weak gravitational lensing and galaxy clustering. These are the most sensitive probes of dark energy and gravity on cosmological scales (see reviews in Peacock et al. 2006; Albrecht et al. 2006, 2009; Weinberg et al. 2013). Combined, they probe the cosmological expansion history, the growth of structure, and the relation between dark and luminous matter.

More detail is provided below, but in summary, to map the three-dimensional matter distribution, *Euclid* aims to determine emission-line redshifts for more than 25 million galaxies over the redshift range  $0.9 < z < 1.8$  using slitless spectroscopy at near-infrared wavelengths<sup>3</sup>. These data provide precise measurements of the growth of structure through the clustering of galaxies and redshift-space distortions, while on large scales the baryon acoustic oscillations (BAOs) probe the expansion history. Simultaneously with the slitless spectroscopy, *Euclid* will collect diffraction-limited<sup>4</sup> images at optical wavelengths over the same area. These enable accurate measurements of the shapes of about 1.5 billion galaxies that will be used to map the distribution of matter using weak gravitational lensing. Photometric

<sup>3</sup> The actual wavelength range covered by the grism is larger, allowing the detection of H $\alpha$  emitters over the redshift range  $0.84 < z < 1.88$  (see Sect. 3.5.3). Throughout this paper, however, we consider the more conservative as-required numbers.

<sup>4</sup> As discussed in more detail in Sect. 7.6.4, the telescope is not a perfect optical system. Hence, in this context, diffraction-limited is to be understood as referring to a telescope of extremely good image quality.

<sup>2</sup> To evaluate the FoM we marginalise over the cosmological and nuisance parameters, while imposing a Gaussian prior on the baryon density from big bang nucleosynthesis (BBN). See Sect. 8.2.3 for more details.

**Table 1.** Fiducial values for the cosmological parameters of the baseline flat  $\Lambda$ CDM cosmological model.

| Cosmological parameter | Fiducial value |
|------------------------|----------------|
| $\Omega_m$             | 0.32           |
| $\Omega_b$             | 0.05           |
| $h$                    | 0.67           |
| $n_s$                  | 0.96           |
| $\sigma_8$             | 0.816          |
| $\sum m_\nu$ (eV)      | 0.06           |
| $\tau$                 | 0.058          |

redshifts for these sources will be determined by combining supporting ground-based observations with near-infrared images in three passbands from *Euclid* over the same area.

As discussed in Laureijs et al. (2011) and more recently by Euclid Collaboration: Blanchard et al. (2020), this particular probe combination can achieve a dark energy FoM  $> 400$  and measure  $\gamma_g$  with an uncertainty of 0.02 ( $1\sigma$ ), where we caution that, to achieve these objectives, the predictions for the observables on small scales need to be improved further (see Sect. 8.2.2). This precision allows us to explore physics beyond the concordance  $\Lambda$ CDM model. These scenarios,  $\Lambda$ CDM with and without spatial curvature, a dynamic dark energy model with an equation of state given by Eq. (1), and a modified gravity scenario based on Eq. (3), provide the basic benchmark cases used to evaluate the performance of *Euclid*. We present updated estimates on the precision that *Euclid* aims to achieve in Sect. 8.2.1.

Apart from distinguishing dark energy and modified gravity models, improving constraints on the cosmological parameters that make up the  $\Lambda$ CDM model provides a crucial consistency test. Currently, local measurements (Riess et al. 2021) of the Hubble constant  $H_0$  show disagreement with the values inferred from the analysis of *Planck* data (Planck Collaboration VI 2020). The high-quality measurements from *Euclid* will help to settle the  $H_0$  debate, because the primary probes of *Euclid* can also provide state-of-the-art constraints on the cosmological parameters that form the baseline flat  $\Lambda$ CDM model; these are listed in Table 1 alongside their fiducial values that are used to assess the performance of *Euclid*.

Historically, these values were chosen based on Table 3 of the 2015 *Planck* results (Planck Collaboration XIII 2016). We consider a baseline fixed sum of neutrino masses  $\sum m_\nu = 0.06$  eV, a fixed optical depth to Thomson scattering from reionisation,  $\tau = 0.058$ , and a spectral index of the primordial density power spectrum,  $n_s = 0.96$ . For the spatially flat  $\Lambda$ CDM model, the dark energy density parameter today,  $\Omega_{DE}$ , is a derived parameter, but we allow it to vary when we consider a model with spatial curvature. For the dimensionless Hubble parameter  $h$  (defined through  $H_0 = 100 h \text{ km s}^{-1} \text{ Mpc}^{-1}$ ), we adopt the CMB value of  $h = 0.67$ . The remaining parameters are  $\Omega_b$  and  $\Omega_m$ , respectively, the baryon and total matter energy densities at the present time, divided by the critical density. Finally,  $\sigma_8$  measures the amplitude of the relative linear density fluctuations within a sphere of radius  $8 h^{-1} \text{ Mpc}$  at the present day. We refer the reader to Euclid Collaboration: Blanchard et al. (2020) for more details on the fiducial choices. *Euclid* will reduce the uncertainties on all these parameters significantly.

*Euclid* will also greatly advance our ability to constrain extensions of the standard cosmological model. In Sect. 8.3 we discuss some cases in more detail, but here we highlight two

specific examples. First, *Euclid* will improve constraints on the sum of neutrino masses. In combination with *Planck*, we expect to reach a precision of  $\sigma(\sum m_\nu) = 0.02$  eV. Second, *Euclid* will improve our understanding of the initial conditions. The concordance model assumes an initial Gaussian random field of perturbations. The parameter  $f_{NL}$  quantifies the quadratic term in the potential (e.g. Matarrese et al. 2000; Dalal et al. 2008), and thus provides a measure for any initial non-Gaussianity, which is encoded in the LSS that *Euclid* will map with unprecedented precision. The aim is to improve over the current measurements from *Planck* (Planck Collaboration IX 2020). Taken together, *Euclid* will test many aspects of the  $\Lambda$ CDM model (Amendola et al. 2018; Euclid Collaboration: Blanchard et al. 2020).

In the remainder of this section we discuss the primary probes in more detail, but we note that the same data enable additional cosmological studies, which are discussed in Sect. 9. Although including this information consistently is not trivial, as highlighted in Laureijs et al. (2011), it is worthwhile to pursue; significant improvement is expected for a wide range of cosmological parameters, but the largest impact is foreseen on the dark energy constraints.

### 2.1. Galaxy clustering

The large-scale clustering of galaxies is one of the most powerful probes of the Universe, carrying crucial information on its mass/energy budget and fundamental parameters. The cosmological information is best extracted by observing the 3D distribution of galaxies in space, combining angular positions with estimates of galaxy distances using the cosmological redshifts from their spectra as a proxy.

This led to the start of systematic redshift surveys that, since the 1970s, have increasingly collected galaxy redshifts over larger and larger volumes. Following the pioneering years of surveys collecting individual spectra from ground-based telescopes (see e.g. Sandage 1975; Rood 1988; Giovanelli & Haynes 1991, for historical reviews), the 1990s saw the emergence of multi-object spectrographs (MOS), which allowed for a quantum leap in survey efficiency. Representative examples of surveys that, in different fashions, exploited MOS spectroscopy for large-scale structure work are the Las Campanas Redshift Survey (LCRS; Shectman et al. 1996), the 2-degree Field Galaxy Redshift Survey (2dFGRS; Colless et al. 2001), the Sloan Digital Sky Survey (SDSS; York et al. 2000), and, more recently and at higher redshifts, the VIMOS Public Extragalactic Redshift Survey (VIPERS; Guzzo et al. 2014; Scodeggio et al. 2018) and the WiggleZ survey (Drinkwater et al. 2018). The SDSS encompasses a number of experiments, including the early *main galaxy* and luminous red galaxy (LRG) samples, and the subsequent Baryon Oscillation Spectroscopic Survey (BOSS; Dawson et al. 2013) and extended-BOSS (eBOSS; Dawson et al. 2016). Similarly, VIPERS represented the final act, for studies of large-scale structure at  $z \sim 1$ , of the deep surveys enabled by the Visible Multi-Object Spectrograph (VIMOS) at the Very Large Telescope (VLT; Le Fèvre et al. 2013).

The *Euclid* NISP slitless spectroscopic survey is part of a new generation of such surveys, which will bring the total number of measured redshifts close to a hundred million. While *Euclid* will sample the  $0.9 < z < 1.8$  redshift range from space, the DESI project (DESI Collaboration 2016), already under way at the Kitt Peak 4-m Mayall telescope, is primarily targeting galaxies at lower redshifts (with significant overlap), using an innovative 5000-fibre automatic positioner. In fact, the wavelength range of its red grisms (Sect. 3.5.3) was specifically

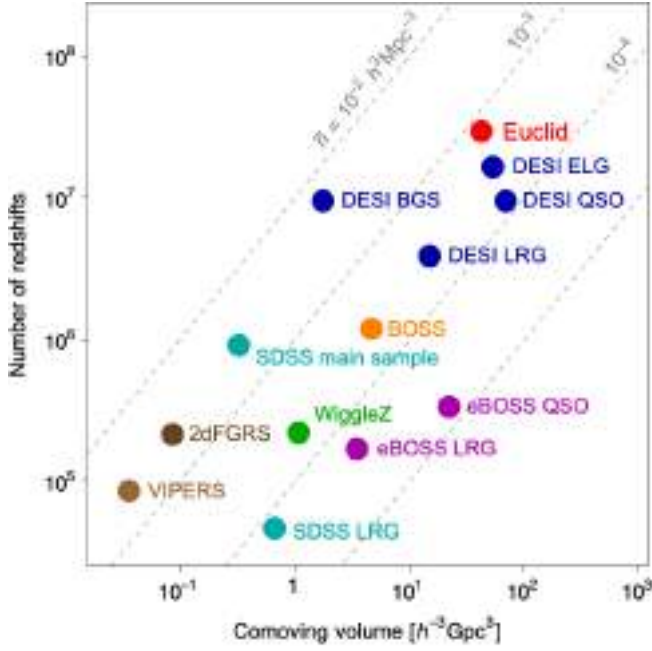


**Fig. 1.** Comparison of the number of redshifts and comoving volume covered by various previous and ongoing spectroscopic surveys against the predictions for *Euclid* (see text for details). The grey lines show lines of constant number density as labelled.

chosen as to make *Euclid* complementary to existing and planned ground-based surveys. The number of expected redshifts and the sampled volume of *Euclid* and DESI are compared with some previous surveys in Fig. 1.

The observed clustering of galaxies within a past lightcone encodes a wide range of physics through a number of processes. The currently favoured picture envisages that the initial comoving pattern of the overdensities that grew to form today's galaxies and large-scale structures was set up in the early Universe, driven initially by inflation (e.g. Bassett et al. 2006). These were then modified before recombination, driven by physics that imprints scales related to the epoch of matter-radiation equality and the propagation of acoustic waves. These are commonly included in models of the power spectrum by a transfer function that multiplies the primordial power-law inflationary spectrum (e.g. Lewis et al. 2000). Shortly after recombination, the density contrast is still small over the scales of interest, perturbations are still linear and their growth is essentially scale-independent. Departures from scale-independence might thus signal the effects of non-zero neutrino mass (an effect of about one per cent is expected with current mass limits – see Lesgourgues & Pastor 2006, for a review), or more exotic physics. Starting from the smallest scales, at late times gravitational evolution becomes nonlinear, bringing in additional information, but also new complications (see, e.g. Bernardeau et al. 2002). As we discuss below, the way that pattern is imprinted into the angles and redshifts measured by a galaxy survey allows us to extract important cosmological information.

Much of this is encoded in the two-point statistics of the overdensity field: in configuration space<sup>5</sup>, we measure the spatial

<sup>5</sup> With *configuration space* we mean the space where we measure galaxy positions and distances, dual to *Fourier space*. In turn, configuration space is distinguished into *real space*, where one uses true galaxy distances and separations are indicated with  $\mathbf{r}$ , and *redshift space*, where distances are derived from measured redshifts, and galaxy separations

two-point correlation function (2PCF) of galaxies,  $\xi_{\text{gg}}(\mathbf{r})$ , which quantifies the excess probability of finding two objects at a given separation  $\mathbf{r}$  with respect to a random Poisson sample tracing the same volume,

$$\langle N_{\text{g},1}(\mathbf{x}) N_{\text{g},2}(\mathbf{x} + \mathbf{r}) \rangle = \bar{n}^2 [1 + \xi_{\text{gg}}(\mathbf{r})] \delta V_1 \delta V_2. \quad (4)$$

Here  $\bar{n}$  is the mean number of galaxies per unit volume and we are considering two small regions, separated by a vector  $\mathbf{r}$ , with volumes  $\delta V_1$  and  $\delta V_2$ , containing  $N_{\text{g},1}$  and  $N_{\text{g},2}$  galaxies, respectively. It is often convenient to measure clustering in Fourier space, and there we measure the power spectrum, which is the Fourier transform of the correlation function:

$$P_{\text{gg}}(\mathbf{k}) = \int_0^\infty d^3 r \xi_{\text{gg}}(\mathbf{r}) e^{i\mathbf{k}\cdot\mathbf{r}}. \quad (5)$$

Our clustering computations use galaxy redshifts to derive their distances. However, redshifts include, in addition to the pure cosmological Hubble flow, the line-of-sight contribution of the galaxy peculiar velocities, induced by density inhomogeneities. This leads to coherent redshift-space distortions (RSDs; Kaiser 1987), introducing an anisotropy in the observed clustering between line of sight (LoS) and transverse separations (see below for more details), such that we measure the clustering in redshift space with separations denoted by  $s$  rather than  $\mathbf{r}$ . Hence, to properly describe (and model) this effect we typically measure the clustering with respect to the LoS. The cosmological information of interest is contained within the first three even power-law moments of the correlation function or power spectrum with respect to  $\mu$ , under the global plane-parallel approximation, where  $\mu$  is constant across a survey and gives the cosine of the angle that a pair of galaxies, for  $\xi(s)$ , or that the Fourier mode wave vector, for  $P(\mathbf{k})$ , makes with respect to the LoS. The first three even Legendre polynomials encode these power-law moments and form an orthonormal basis:

$$\mathcal{L}_0(\mu) = 1; \quad (6)$$

$$\mathcal{L}_2(\mu) = \frac{1}{2} (3\mu^2 - 1); \quad (7)$$

$$\mathcal{L}_4(\mu) = \frac{1}{8} (35\mu^4 - 30\mu^2 + 3). \quad (8)$$

We therefore typically decompose the clustering into the Legendre polynomial moments of the correlation function and power spectrum (Hamilton 1998):

$$\xi_\ell(s) = (2\ell + 1) \int_{-1}^1 d\mu \xi_{\text{gg}}(s) \mathcal{L}_\ell(\mu), \quad (9)$$

$$P_\ell(k) = (2\ell + 1) \int_{-1}^1 d\mu P_{\text{gg}}(\mathbf{k}) \mathcal{L}_\ell(\mu), \quad (10)$$

with  $\ell = 0$  corresponding to the monopole,  $\ell = 2$  the quadrupole, and  $\ell = 4$  the hexadecapole moment. In practice, the LoS varies across a survey, and we typically make a local-plane parallel approximation, where we assume that the LoS is the same for each pair of galaxies analysed. In this case, the statistic we wish to measure is that given in Eq. (9), but the method by which we estimate it is not as simple as this equation suggests, as discussed in more detail in Sect. 7.7.1. A prediction for the power spectrum

are typically indicated with  $s$ . Correspondingly, the same distinction applies to the Fourier side, where wavenumbers  $\mathbf{k}$  can be defined in real and redshift space. Again, redshift-space quantities are usually indicated with the subscript  $s$ .

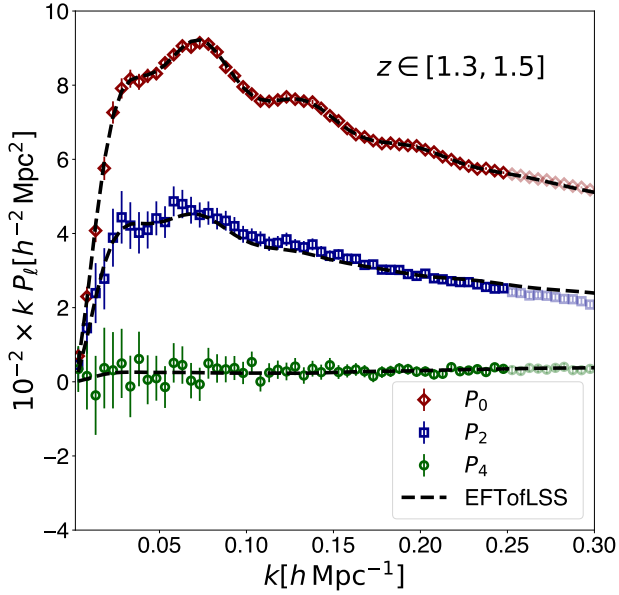


**Fig. 2.** Measured galaxy power spectrum multipoles calculated from dedicated mocks (Pezzotta et al. in prep.) based on the Flagship simulation (see Sect. 6.1) of the *Euclid* emission-line sample for a redshift bin  $1.3 < z < 1.5$ , compared to a best-fit model based on effective field theory (EFT, also called EFTofLSS, see Sect. 8.2.2 for further discussion) assuming  $k_{\max} = 0.25 h \text{ Mpc}^{-1}$ . Error bars here correspond to the *Euclid* full mission volume for this redshift bin prior to observational effects.

moments to be measured by *Euclid* is given in Fig. 2. This figure shows measurements on mock catalogues based on the Euclid Flagship simulation (see Sect. 6.1), and a best-fit model that is able to predict the clustering into the nonlinear regime (see Sect. 8.2.2 for more details).

The most robust (and easy to isolate) signal in the pattern of galaxies are the so-called Baryonic Acoustic Oscillations (BAOs), a series of peaks and troughs in the power spectrum caused by acoustic waves during the pre-recombination era (e.g. Eisenstein & Hu 1998; Meiksin et al. 1999). These are evident in the monopole of Fig. 2. The acoustic waves push baryonic material out from initial perturbations to the baryon-drag scale, which is linked to the comoving sound horizon at recombination. When analysed in Fourier space this results in a sinusoidal term in the transfer function, depending on whether the movement of material cancels or reinforces that from other perturbations separated by the wavenumber of interest. The BAOs observed have the same physical origin as the oscillations seen in the CMB anisotropy power spectrum (Planck Collaboration VI 2020), and were first observed in the 2dFGRS (Percival et al. 2001; Cole et al. 2005) and SDSS (Eisenstein et al. 2005) surveys. Hardware improvements made to the Sloan telescope enabled BOSS to provide the first  $5\sigma$  measurement of BAOs from the largest volume of the Universe obtained at that point (Anderson et al. 2012). The extended-BOSS project pushed these BAO observations to higher redshifts (Alam et al. 2021). The BAO are largely insensitive to galaxy bias, simplifying their modelling.

The power of BAOs in a galaxy survey results from using them as a standard ruler undergoing expansion that is comoving with the average expansion of the Universe. The observed wavenumbers of BAOs constrains the ratio  $r_d/D_H(z)$  in the radial direction, and  $r_d/D_A(z)$  in the transverse direction, where  $r_d$  is the sound horizon at the end of the drag epoch,  $D_H(z) = c/H(z)$  is the Hubble distance, and  $D_A(z)$  is the angular-diameter

distance. The different dependencies along and across the LOS lead to a very clean geometrical measurement: the correct set of cosmological parameters will be the one leading to a statistically isotropic clustering requiring the product  $H(z)D_A(z)$  to match the truth. This is known as the Alcock-Paczynski (AP; Alcock & Paczynski 1979) effect and the principle holds for features in the power spectrum other than BAOs; for example it can also be applied to stacks of objects such as voids, which are underdense regions defined by a specific threshold (see Pisani et al. 2019, for a review). With the unprecedented volume of the Wide survey, void statistics with *Euclid*, such as the void size function and the void-galaxy cross-correlation function are expected to deliver competitive, complementary cosmological constraints (see Verza et al. 2019; Hamaus et al. 2022; Contarini et al. 2022; Bonici et al. 2023; Radinović et al. 2023, for specific forecasts).

The BAOs are just one feature within the full power spectrum of the galaxy distribution. The shape of the galaxy power spectrum underlying the BAO depends on cosmology through the spectral index of the fluctuations coming from inflation  $n_s$  and the matter-radiation horizon scale, which depends on the parameter combination  $\Omega_m h$ . The full power spectrum predicted to be observed by *Euclid* is shown in Fig. 2 in terms of its Legendre multipoles.

While BAOs carry information about the expansion history  $H(z)$  and thus the equation-of-state parameter of dark energy  $w(z)$ , the anisotropy of the clustering pattern produced by RSDs, mentioned earlier, provides us with complementary, potentially powerful information on the growth rate of structure  $f_g(z)$ . As discussed in the introduction to this section, combined precise measurements of  $w(z)$  and  $f_g(z)$  are key to understand the origin of cosmic acceleration, potentially discriminating between dark energy and modifications of GR, a major goal of *Euclid*. The confidence in the use of RSDs as a test of dark energy consolidated at the time of the ESA Cosmic Vision 2020–2025 call (Guzzo et al. 2008; Wang 2008a). In fact, the use of RSDs as a primary cosmological probe was one key original ingredient in the SPACE proposal (Cimatti et al. 2009), which eventually became the spectroscopic experiment on board *Euclid* (also see Wang et al. 2010). Since then, virtually all redshift surveys have been including RSDs as a standard probe of the growth rate of structure (see Alam et al. 2017, 2021, and references therein). In practice, the growth rate is derived from RSDs by modelling the measured anisotropy of the correlation function or power spectrum, as quantified by their multipoles, which depends on the combination  $f_g(z)g_+(z)\sigma_8$  (Percival & White 2009).

In galaxy clustering measurements,  $g_+(z)\sigma_8$  is degenerate with the so-called ‘galaxy bias’, that is the unknown amplification with respect to the clustering of the underlying matter density field. This is expected to arise naturally if galaxies form at the peaks of the density-fluctuation field (Kaiser 1984), with additional complications and scale-dependence on small scales (see Desjacques et al. 2018, for an extensive review). There, comoving galaxy separations no longer match those between the seed perturbations from which their hosting dark matter halos grew. Galaxy formation and evolution inside halos adds a further layer of complication, that is a galaxy-halo bias. On very large scales the galaxy bias signal can depend on the level of primordial non-Gaussianity, typically enabling a measurement of the  $f_{\text{NL}}$  parameter. Except for the deviation caused by the  $f_{\text{NL}}$  signal, we expect the large-scale bias of galaxies to tend towards the scale-independent deterministic linear value predicted by a pure statistical peak (halo) to background (matter) bias. In that case the galaxy power spectrum is simply proportional to the matter power spectrum,  $P_{\text{gg}}(\mathbf{k}) = b_1^2 P_{\text{m}}(\mathbf{k})$ .

The statistical properties of a Gaussian random field are completely described by its two-point correlation function or, equivalently, the power spectrum. This is not the case for the galaxy distribution which is highly non-Gaussian as it is shaped by several nonlinear processes, such as gravitational instability, redshift-space distortions, and galaxy biasing. Higher-order clustering statistics, starting from the galaxy three-point function in configuration space, or the bispectrum in Fourier space, are the direct result of these nonlinear effects. Recent studies have demonstrated that performing a joint analysis of two- and three-point statistics of the galaxy distribution is key to disentangling the impact of these nonlinearities from the signatures of new physics. This is expected to improve constraints on the cosmological parameters by 10–30% (Yankelevich & Porciani 2019). In addition, there are models of inflation that can only be constrained using higher-order statistics (e.g. D’Amico et al. 2025). To take advantage of this additional information, we will measure the redshift-space multipoles for both the three-point function and the bispectrum (also see Sect. 9) and analyse them jointly with two-point statistics as a natural extension of all probes and methods mentioned above.

The signatures of the physical processes discussed above can lead to strong degeneracies between measurements, for example, between the AP effect and RSDs (Ballinger et al. 1996). Thus it is important to measure them together, and to mitigate the effects of galaxy bias (see Sect. 8.2.2). The relative robustness of using the BAO signature as a standard ruler means that it is often advantageous to extract this information separately. This is commonly achieved by fitting a model where polynomial or similar terms are added in order to isolate the BAO feature in the power spectrum (Beutler et al. 2017) or correlation function (Ross et al. 2017). The scale of the BAO signal is then extracted and used directly to constrain models. The precision with which the BAO scale can be measured can be improved by a technique called reconstruction (Eisenstein et al. 2007), where the nonlinear motions of galaxies are estimated from the galaxy field, and used to find the positions of the initial overdensities. This sharpens the BAO signal, increasing the precision of the determination of the centroid.

The galaxy-clustering probe uses overdensities in the galaxy field as a direct probe of cosmology and thus is sensitive to non-cosmological effects that alter observed densities. In order to use galaxy surveys one has to understand their specific selection function, so as to define a mask or window that describes where galaxies can be found. Typically, because of the windows’ complexity, this is usually quantified by making use of random catalogues, Poisson sampling the expected density. The overdensity is then extracted by comparing galaxy and random catalogues (see Sect. 7.7.1 for a description of how these will be created). Typical problems in the analysis of galaxy surveys arise from the selection of the galaxy sample, which can be distorted by Galactic extinction or stellar density (Ross et al. 2012). For example, areas near bright stars are unusable and must be masked. If these changes in the observed density are not corrected by matching the weighted galaxy field to the weighted random field, then the spatial distribution of bright stars may be imprinted in the overdensities in our map of the Universe and misinterpreted as a cosmological signal. Space-based slitless spectroscopy helps to reduce the impact of many of these effects. In particular, no target sample is required to be selected from ground-based imaging data. On the other hand, this requires careful understanding of the potential density-dependent systematic effects that could arise due to confusion among faint spectra in crowded areas. Considerable effort has

been invested to understand and model these effects through end-to-end simulations.

The cosmological information available from the galaxy field is simplest to extract where the physics can be explained by linear processes. On small scales, gravity induces nonlinearities in the distribution of density. It is possible that by studying particular locations in the density field, such as voids or clusters, the linear information on small scales may be easier to extract than from the field as a whole. For example, the relation between the overdensity and velocity field near voids is thought to be close to linear (Hamaus et al. 2014). For the AP effect, we can extract additional information from the fact that a stack of voids should be spherical on average (e.g. Woodfinden et al. 2023). Thus, in addition to the galaxy field, *Euclid* will study these special places in the Universe to obtain further, complementary cosmological information.

## 2.2. Weak gravitational lensing

As demonstrated in the previous section, galaxies are powerful, but biased, tracers of the LSS. To fully exploit the statistical power of the density modes traced by the galaxies, we need to link their properties to the surrounding matter structures. Hence, a direct measurement of the (predominantly dark) matter distribution provides not only important information on how galaxies populate halos, but also probes the growth of large-scale structures. Conveniently, such a measurement is possible thanks to the observable effects of gravitational lensing: massive structures distort space-time, warping the paths of photons. If the deflections are sufficiently large, multiple images of distant galaxies are formed. Such cases of strong gravitational lensing can be used to study the matter distribution on small scales, or exploited as cosmic magnifying glasses (see Sect. 9.3 for some applications).

Generally, the deflections of single objects cannot be measured. However, the matter distribution, via its tidal gravitational field, gives rise to small coherent distortions in the shapes of distant galaxies. This change in the observed galaxy shapes is called weak gravitational lensing (for thorough introductions, see Mellier 1999; Bartelmann & Schneider 2001; Bartelmann 2010). In particular, the weak lensing shear, which describes the weak lensing-induced difference in the galaxies’ observed ellipticity<sup>6</sup> contains information on the cosmic matter distribution. This shear is small compared to the intrinsic ellipticities of galaxies, and ensembles of galaxies need to be averaged to reveal the coherent patterns that can be used to map the distribution of matter along the LoS (Kaiser & Squires 1993, also see Sect. 7.7.3). The weak lensing signal was first detected around massive clusters of galaxies (Tyson et al. 1990) and its potential for cosmology was quickly recognised (e.g. Blandford et al. 1991; Miralda-Escude 1991; Kaiser 1992; Bernardeau et al. 1997) as the shape correlations provide statistical information about the cosmic LSS, which, in turn, depends on the cosmic expansion history and structure growth (see e.g. Kilbinger 2015, for a recent review). This led to the first deep imaging campaigns to measure weak lensing by LSS, or cosmic shear, with the first unambiguous detections reported nearly simultaneously by Bacon et al. (2000), Kaiser et al. (2000), Van Waerbeke et al. (2000), Wittman et al. (2000). Since then, weak lensing has become an established tool to infer cosmological parameters and

<sup>6</sup> As is common in the weak lensing literature, we refer to the quantity describing the shape of a galaxy as ‘ellipticity’. Mathematically, this ellipticity corresponds to the third flattening of the galaxy image.

has been successfully applied to ever larger surveys, such as the Hyper Suprime-Cam (HSC; [Aihara et al. 2018](#)), the Kilo-Degree Survey (KiDS; [Kuijken et al. 2015](#)), and the Dark Energy Survey (DES; [Abbott et al. 2016](#); [Becker et al. 2016](#)).

The weak lensing signal can be decomposed into a curl-free  $E$ -mode and a gradient-free  $B$ -mode component ([Crittenden et al. 2002](#); [Schneider et al. 2002a](#)). To first order, weak lensing by the LSS only causes  $E$ -modes, while  $B$ -modes can be caused by systematic and astrophysical effects (e.g. [Heavens et al. 2000](#); [Schneider et al. 2002b](#); [Hoekstra 2004](#)). Usually, the  $E$ -mode signal is used for cosmological analysis, while the  $B$ -mode signal is a probe of unmodelled systematic effects (e.g. [Hilbrandt et al. 2017](#); [Asgari & Heymans 2019](#)).

For cosmic shear studies, key observables are the two-point shear correlation functions  $\xi_+(\theta)$  and  $\xi_-(\theta)$ , which correlate the estimates for the shear components of pairs of distant galaxies at angular positions  $\boldsymbol{\theta}$  and  $\boldsymbol{\theta}'$ , respectively, so that

$$\xi_{\pm}(\theta) = \langle \gamma_t(\boldsymbol{\theta}) \gamma_t(\boldsymbol{\theta}') \rangle \pm \langle \gamma_{\times}(\boldsymbol{\theta}) \gamma_{\times}(\boldsymbol{\theta}') \rangle, \quad (11)$$

where  $\gamma_t$  and  $\gamma_{\times}$  are the tangential and cross-component of the shear, defined with respect to the separation  $\theta$  between the galaxies. The shear correlation functions are related<sup>7</sup> to the  $E$ - and  $B$ -mode shear power spectra  $C^{EE}(\ell)$  and  $C^{BB}(\ell)$  as ([Chon et al. 2004](#); [Lemos et al. 2017](#); [Kilbinger et al. 2017](#); [Kitching et al. 2017](#))

$$\xi_{\pm}(\theta) = \sum_{\ell \geq 2} \frac{2\ell + 1}{4\pi} [C^{EE}(\ell) \pm C^{BB}(\ell)] d_{2\pm 2}^{\ell}(\theta), \quad (12)$$

where  $d_{2\pm 2}^{\ell}$  is the Wigner- $d$  function. In turn,  $C^{EE}$  is related to the matter power spectrum  $P_m(k, z)$ . Under the flat-sky approximation this relation reduces to Hankel transforms,

$$\xi_{\pm}(\theta) \simeq \int_0^{\infty} \frac{d\ell \ell}{2\pi} J_{0/4}(\ell \theta) [C^{EE}(\ell) \pm C^{BB}(\ell)], \quad (13)$$

where the  $J_y$  are Bessel-functions of the first kind and  $J_0$  is used for  $\xi_+$  and  $J_4$  for  $\xi_-$ . Neglecting  $B$ -modes, a simple form of the relation between  $C^{EE}$  and  $P_m$  can be derived by assuming the Limber approximation ([Limber 1953](#); [Kaiser 1998](#)), and a spatially flat Universe (see [Taylor et al. 2018b](#), for a generalisation beyond this assumption) as

$$C^{EE}(\ell) = [L^{\gamma}(\ell)]^2 \int_0^{\infty} dz \frac{c}{H(z)} \left[ \frac{W^{\gamma}(z)}{\chi(z)} \right]^2 P_m \left[ \frac{\ell + 1/2}{\chi(z)}, z \right], \quad (14)$$

where the prefactor,

$$L^{\gamma}(\ell) = \sqrt{\frac{(\ell + 2)!}{(\ell - 2)!}} \left( \frac{2}{2\ell + 1} \right)^2, \quad (15)$$

comes partly from the conversion from the spectrum of the lensing potential to that of shear  $E$  modes, and partly from the Limber approximation (see [Lemos et al. 2017](#); [Kilbinger et al. 2017](#); [Kitching et al. 2017](#), for derivations of these expressions,

<sup>7</sup> To simplify the discussion, we ignore the fact that the observed ellipticities provide an estimate for the reduced shear  $g \equiv \gamma/(1 - \kappa)$ , where  $\kappa$  is the convergence (see e.g. [Schneider & Seitz 1995](#); [Bartelmann & Schneider 2001](#), for more details). We also implicitly ignore intrinsic alignments. In the actual analysis of *Euclid* data, these, and several other subtle complications, will need to be accounted for [Euclid Collaboration: Deshpande et al. \(2024\)](#).

and relaxation of the approximations). Above,  $\chi(z)$  is the comoving distance at redshift  $z$ , and  $W^{\gamma}(z)$  is the lensing efficiency kernel,

$$W^{\gamma}(z) = \frac{3\Omega_m H_0^2}{2c^2} \chi(z)(1+z) \int_z^{\infty} dz' n(z') \frac{\chi(z') - \chi(z)}{\chi(z')}, \quad (16)$$

for a sample of sources with a redshift distribution  $n(z)$ <sup>8</sup>. Hence, the interpretation of the observed lensing signal depends on knowing the redshift distribution of the source galaxies. Although redshifts for individual galaxies are not required, the sensitivity to cosmological parameters is rather limited when a single set of sources is used.

To exploit the information on the evolution of the LSS over cosmic time, key to constraining the dark energy equation of state parameter,  $w(z)$ , the sources need to be divided into narrow redshift bins that, ideally, do not overlap. Combined, the bins provide tomographic information on the matter distribution along the LoS. A finer tomographic binning increases the redshift resolution, but also leads to a decrease of the signal-to-noise ratio in each individual bin as it contains fewer galaxies. Moreover, as the sources in different bins probe the same structures at lower redshifts, the resulting lensing signals are highly correlated, and the statistical gain saturates quickly ([Ma et al. 2006](#)).

A tomographic analysis requires redshift estimates for the individual sources, which are too faint and too numerous for dedicated spectroscopic follow-up. Fortunately, photometric redshifts ([Koo 1985](#); [Loh & Spillar 1986](#); [Newman & Gruen 2022](#)) can be used, provided their precision is substantially better than the width of the tomographic bins. In the case of *Euclid*, we aim to divide the source sample into as many as 13 bins in the range  $0.2 \leq z \leq 2.5$ . To achieve these objectives, the standard deviation  $\sigma_z$  of the photometric redshift estimates needs to satisfy  $\sigma_z < 0.05(1+z)$ , while the catastrophic failure rate needs to be less than 10% ([Amara & Réfrégier 2007](#); [Laureijs et al. 2011](#)). To meet these stringent requirements, *Euclid* complements the VIS data with deep space-based near-infrared (NIR) photometry in three bands; we also take additional, uniform photometry from the ground (see Sect. 4.4). Moreover, to obtain accurate cosmological parameter estimates, the mean galaxy redshifts within the bins need to be known with an accuracy  $\sigma_{\langle z \rangle} < 0.002(1+z)$  ([Ma et al. 2006](#); [Amara & Réfrégier 2007](#); [Kitching et al. 2008b](#)). As discussed in more detail in Sect. 7.6.1, this drives the need for extensive spectroscopy that fully samples the colour-redshift space (e.g. [Masters et al. 2015](#)).

Such relatively narrow redshift bins offer a powerful handle on the time evolution of the cosmic shear spectra. It allows us also to take full advantage of the so-called Bernardeau–Nishimichi–Taruya (BNT) transformation ([Bernardeau et al. 2014](#); [Taylor et al. 2018a, 2021](#), also see Sect. 8) with which scale mixing from projection effects can be fully controlled. This has major benefits for the interpretation of the weak lensing signal from theoretical models and the modelling of astrophysical systematic effects ([Taylor et al. 2021](#)). Another motivation for the fine binning is the need to combine the lensing measurements with the angular positions of galaxies in a so-called ‘3×2pt’ analysis, discussed in Sect. 2.3.

The shear correlation functions (and convergence power spectra) primarily depend on the square of the parameter  $S_8 \equiv \sigma_8 \sqrt{\Omega_m/0.3}$  in the linear regime, and to higher orders of  $S_8$  at smaller scales. (e.g. [Hall 2021](#)). The degeneracy between  $\Omega_m$  and

<sup>8</sup> Note that  $n(z)$  has to be normalised to unit area, that is,  $\int dz n(z) = 1$ .

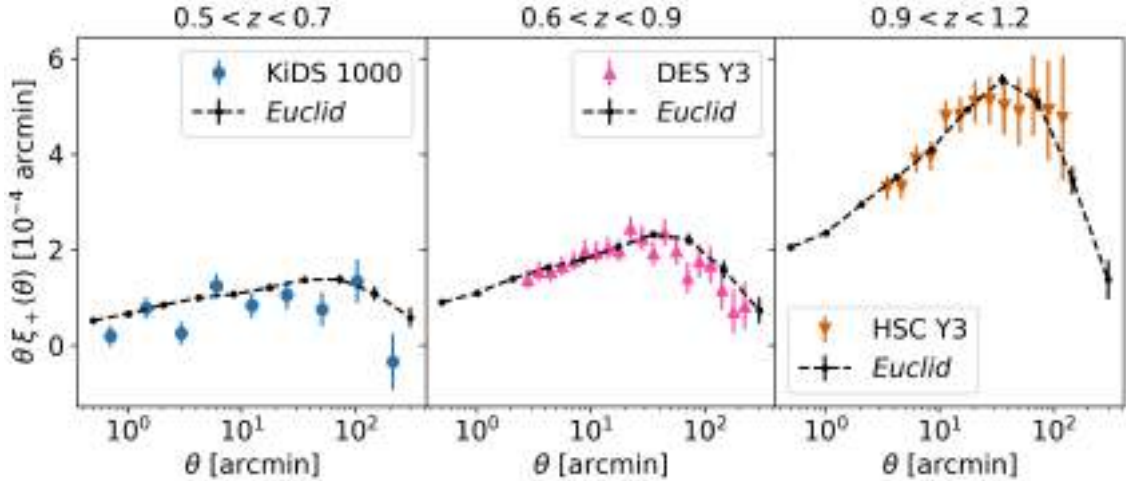


**Fig. 3.** Shear correlation function  $\xi_+(\theta)$  for KiDS-1000 (left, from [Asgari et al. 2021](#)), DES Y3 (middle, from [Amon et al. 2022](#)), and HSC Y3 (right, from [Li et al. 2023b](#)), and expected for *Euclid*. Each panel uses sources distributed according to the tomographic bin with the highest S/N of the respective survey. The S/N for *Euclid* is an order of magnitude larger than that of the most recent surveys. The other shear correlation function  $\xi_-(\theta)$  shows a similar improvement in S/N (not shown).

$\sigma_8$  is broken by nonlinear corrections or with the use of higher-order statistics ([Bernardeau et al. 1997](#)). Cosmic shear analyses of current surveys at the time of writing have already tightly constrained  $S_8$  with a precision of 2–4% (e.g. [Asgari et al. 2021](#); [Amon et al. 2022](#); [Li et al. 2023b](#)). Interestingly, the reported values are consistently lower than the one inferred from the cosmic microwave background with *Planck*. The current level of disagreement for individual measurements ranges from 2 to  $3\sigma$ , but it remains to be seen if this points to a problem with the cosmological standard model ([Di Valentino et al. 2021](#)).

Cosmic shear is also sensitive to the cosmic expansion history and the dark energy equation of state through the angular-diameter distances between the observer, the distorted source galaxies, and the lensing matter structures; changes in the projection of structures along the LoS; and the decay in gravitational potentials as the expansion accelerates. Current cosmic shear analyses lack the statistical constraining power to provide meaningful constraints on the dark energy equation of state. This will change with *Euclid*, since it will achieve more than an order-of-magnitude increase in precision compared to previous surveys ([Euclid Collaboration: Blanchard et al. 2020](#)), owing to its depth, precise shear measurements, large area, and high galaxy density.

The statistical uncertainty of weak lensing measurements is primarily limited by sample variance and shape noise, both of which will be immensely reduced by *Euclid*. The Euclid Wide Survey (EWS, see Sect. 4) will cover an area 3 times larger than the final DES release, the largest deep imaging survey to date, suppressing sample variance. Additionally, since *Euclid* has greater depth than previous surveys, it effectively probes a larger volume of the Universe. *Euclid* is expected to detect about 2 billion source galaxies for which shapes can be measured, several orders-of-magnitude more than current surveys, thereby reducing shape noise. Given that many of these galaxies are at higher redshifts than those used in previous surveys, the observed galaxies typically exhibit larger lensing signals, further enhancing the signal-to-noise ratio. These strengths, particularly its depth, accurate shear measurements, and large galaxy numbers, will help *Euclid* to achieve a significant increase in precision compared to previous surveys (see [Amara & Réfrégier 2007](#), for the scaling of the FoM with these survey parameters), while the sharp point spread function (PSF) reduces the detrimental

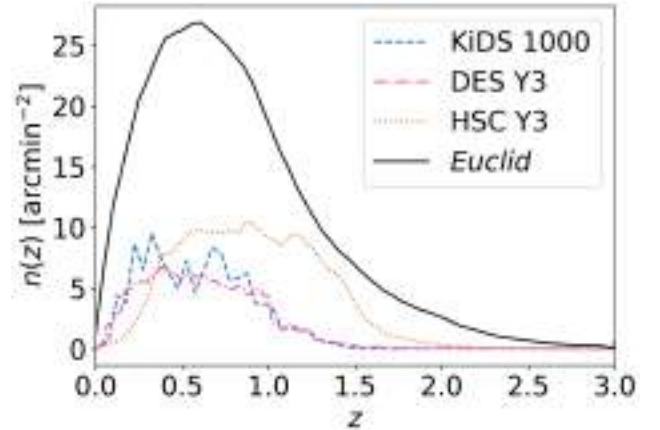


**Fig. 4.** Source-redshift distributions  $n(z)$  of the KiDS, DES, and HSC, and as expected for *Euclid*. Distributions are normalised to the mean number density of sources used in the lensing analyses.

impact of blending on the shape measurements ([MacCrann et al. 2022](#); [Li et al. 2023a](#)).

This is illustrated in Fig. 3, where we show shear correlation functions  $\xi_+(\theta)$  measured by the KiDS ([Asgari et al. 2021](#)), DES ([Amon et al. 2022](#)), and HSC ([Li et al. 2023b](#)). Each panel shows  $\theta\xi_+(\theta)$  for the tomographic bin with the highest S/N for each survey. Error bars are the square root of the diagonal elements of the cosmic shear covariances, including shape noise and sample variance. For *Euclid*, these were computed with the OneCovariance-code<sup>9</sup> ([Reischke et al., in prep.](#)). Comparing with the predictions for *Euclid* in the same tomographic bin, we expect an order of magnitude increase in S/N thanks to the combination of a higher galaxy number density and the increase in survey area.

The increase in galaxy number density is also apparent from Fig. 4, which demonstrates another advantage of *Euclid* compared to previous surveys, namely its increased redshift range. The amplitude of the lensing signal rapidly increases as

<sup>9</sup> <https://github.com/rreischke/OneCovariance>; it uses the same prescription as [Joachimi et al. \(2021\)](#), which is similar to [Euclid Collaboration: Sciotti et al. \(2024\)](#) and [Upham et al. \(2022\)](#).

a function of source redshift (Bernardeau et al. 1997), so that even a modest increase in number density of higher redshift sources can lead to a significant improvement in constraining power. The figure compares the redshift distribution of KiDS (Hildebrandt et al. 2021), DES (Myles et al. 2021), and HSC (Rau et al. 2023), to the expected redshift distribution for *Euclid*, obtained by selecting galaxies with  $I_E \leq 24.5$  in the Flagship 2 simulation (see Sect. 6.1). Shape measurements in KiDS and DES are essentially limited to galaxies at  $z < 1.2$ . The deep HSC data allow for a significant number of galaxies at redshifts between 1 and 1.5, but only *Euclid* will obtain a meaningful number of sources at higher redshifts. This larger redshift range is crucial for determining the evolution of dark energy.

To exploit the unprecedented statistical power of *Euclid*, it is essential that instrumental sources of bias are much smaller than the measurement uncertainties. Moreover, the exquisite measurements need to be complemented with accurate modelling of cosmological and astrophysical effects. Systematic effects for weak lensing arise, for example, from imperfect shape measurements and biases in the estimation of the source redshift distribution. We refer the interested reader to the review by Mandelbaum (2018) for a more in-depth discussion.

The observed images are modified by the telescope optics: even for space-based observations the blurring by the PSF is a dominant source of bias that needs to be accounted for. Moreover, imperfections in the detector introduce additional changes in the images, while cosmic rays pose another challenge. Considering the estimated shear  $\hat{\gamma}$  and the true shear  $\gamma$  as complex numbers, their difference can be expressed to first order (see Kitching et al. 2020) as

$$\hat{\gamma} - \gamma = m_0^{\text{bias}} \gamma + m_4^{\text{bias}} \gamma^* + c^{\text{bias}} + n, \quad (17)$$

where  $m_0^{\text{bias}}$  and  $m_4^{\text{bias}}$  are spin-0 and spin-4 complex operators, respectively, and the asterisk denotes complex conjugation. The value of  $m_0^{\text{bias}}$  quantifies the dilation and rotation of the true shear, whereas  $m_4^{\text{bias}}$  allows for a reflection around the axis determined by its phase (Euclid Collaboration: Congedo et al. 2024).  $c^{\text{bias}}$  is the additive bias, while  $n$  corresponds to the random (shape) noise in the shear estimate.

The biases depend on the instrument, the shape measurement method (e.g. Heymans et al. 2006; Hoekstra et al. 2017, 2021), and galaxy properties, in particular the size and signal-to-noise ratio (e.g. Hoekstra et al. 2015). They can also vary spatially, but  $C^{EE}$  is affected principally only by the mean multiplicative bias<sup>10</sup> and the correlation between the shear field and the additive bias (Kitching et al. 2019, 2021).

Given a survey design, it is possible to derive limits on the shear biases that can be tolerated (Amara & Réfrégier 2008). These can be specified further by exploring how errors in the estimate of the PSF propagate (Paulin-Henriksson et al. 2009; Massey et al. 2013), as well as other sources of bias. The detailed breakdown presented in Cropper et al. (2013) formed the basis for the development of the shape measurement pipeline for *Euclid*, which is discussed in more detail in Sect. 7.6.

To realise the full statistical potential of *Euclid*, we require the uncertainty on the multiplicative bias to be less than  $2 \times 10^{-3}$ , and the uncertainty on the additive bias to be less than  $1.5 \times 10^{-4}$  (Cropper et al. 2013). Recent studies (Euclid Collaboration: Paykari et al. 2020; Kitching et al. 2019) have shown that we

<sup>10</sup> Recently, Kitching & Deshpande (2022) highlighted that any nonlinearity in the relation between the true and estimated shear needs to be quantified and possibly accounted for.

need to distinguish between sources of bias that are constant across the survey and spatially varying effects. Although these refinements can provide margin for specific instrumental effects, the baseline requirements provided an excellent basis for the hardware and software development needed for the mission.

Because we aim to push the limits of what can be done within the mission constraints, the measurements are challenging, despite the advantages that a space telescope brings. Compared to ground-based surveys the main benefit of *Euclid* is that the PSF residuals scale with the square of the PSF size (Paulin-Henriksson et al. 2009; Massey et al. 2013). This reduces the baseline multiplicative bias for *Euclid* compared to ground-based telescopes, which cannot avoid the blurring of the images by atmospheric turbulence. Nonetheless, the PSF needs to be known with unprecedented accuracy. A complication is that we need to account for the fact that the PSF is a strong function of wavelength, and therefore depends on the spectral energy distribution (SED) of each individual galaxy (Cypriano et al. 2010; Eriksen & Hoekstra 2018), which can also vary spatially (Voigt et al. 2012; Semboloni et al. 2013a; Er et al. 2018). The challenges in modelling the PSF and measuring the shapes of galaxies are discussed in Sects. 7.6.4 and 7.6.5, respectively.

Since the weak lensing observables provide unbiased estimates of the projected matter distribution, it was believed that the interpretation of the lensing signal would be relatively immune to astrophysical processes. However, it has become clear that this is not the case, especially at the precision of *Euclid*. First of all, the intrinsic shapes of galaxies are correlated with each other and their surrounding matter distribution due to tidal interactions during their formation. This intrinsic alignment (IA) effect needs to be accounted for, because it causes spurious signals in the cosmic shear signal and the position-shear correlations (Joachimi et al. 2015; Kirk et al. 2015; Troxel & Ishak 2015). On large scales, tidal alignment models provide a description of the scale dependence (e.g. Hirata & Seljak 2004; Bridle & King 2007; Blazek et al. 2019), but the amplitude of the IA signal cannot be predicted from first principles because it depends on the complex process of galaxy formation. Moreover, the signal depends on galaxy type, galaxy luminosity, and redshift. Although observations can be used to constrain the predicted amplitude (Fortuna et al. 2021), our current knowledge of the IA signal is insufficient. *Euclid* itself will be a great resource for direct measurements, but the modelling of the IA signal is likely to remain an active area of research for the foreseeable future.

The second complication is that non-gravitational processes, such as heating by active galactic nuclei, supernovae, or star formation, redistribute baryons. To explain current observations, models of galaxy formation require that a significant fraction of the baryons are expelled, leading to a suppression of the matter power spectrum (van Daalen et al. 2011; Debackere et al. 2020). Neglecting these processes can significantly bias cosmological parameter constraints (e.g. Semboloni et al. 2011, 2013b; Chisari et al. 2019). In principle, the changes in the matter distribution can be modelled using hydrodynamical simulations (e.g. Schaye et al. 2010; Le Brun et al. 2014; McCarthy et al. 2017), physically motivated modifications to analytical halo models (e.g. Debackere et al. 2020; Mead et al. 2021), or ‘baryonification’ models that modify halos in gravity-only simulations according to prescribed gas content (Schneider & Teyssier 2015; Schneider et al. 2019; Aricò et al. 2020). The challenge is to decide which models capture the feedback processes correctly, although the findings of van Daalen et al. (2020) suggest it may be possible to describe the effect of feedback on the matter power spectrum with only a few nuisance parameters that need to be marginalised

over when estimating the cosmological parameters. Finally, several simplifying assumptions in the modelling of the observed cosmic shear power spectrum need re-evaluation for *Euclid*, such as an increased source galaxy density due to weak lensing magnification (magnification bias), the exclusion of blended galaxy pairs (source obscuration), and local over- or under-densities (Euclid Collaboration: Deshpande et al. 2024).

### 2.3. Photometric $3 \times 2$ pt analysis

Although cosmic shear is a powerful probe of cosmology, it cannot reach a FoM  $> 400$  by itself (Laureijs et al. 2011; Euclid Collaboration: Blanchard et al. 2020). To unlock the full constraining power of *Euclid*, we need to combine the cosmic shear correlation functions,  $\xi_{\pm}(\theta)$ , with the galaxy angular correlation function,  $w(\theta)$ , and the cross-correlations between galaxy angular positions and the tangential component of the ellipticities of background galaxies,  $\langle \gamma_t \rangle(\theta)$ . These additional two-point functions are commonly referred to as ‘photometric galaxy clustering’ and ‘galaxy-galaxy lensing’ or ‘shear-clustering cross-correlation’, respectively.

Equivalently, angular power spectra can be measured and used for the analysis. Hence, Eq. (14) can be generalised to encompass all three probes,

$$C_{ij}^{AB}(\ell) = L^A(\ell) L^B(\ell) \quad (18)$$

$$\times \int_0^{\infty} dz \frac{c}{H(z)} \frac{W_i^A(z) W_j^B(z)}{\chi^2(z)} P_m \left[ \frac{\ell + 1/2}{\chi(z)}, z \right].$$

In the expression above,  $A$  and  $B$  label the probes being correlated, while  $i$  and  $j$  indicate the tomographic bins considered. In the case of shear,  $L^\gamma$  is given by Eq. (15), whereas  $L^g(\ell) = 1$ . For instance, for  $A = B = \gamma$  and  $i = j$ , we obtain Eq. (14). Alternatively, it is possible to include intrinsic alignments by using the ellipticity power spectrum (Euclid Collaboration: Blanchard et al. 2020). For photometric galaxy clustering, we take  $A = B = g$  and, assuming a linear galaxy bias,

$$W_i^g(z) = \frac{H(z)}{c} b_{\text{gal}}(z) n_i(z), \quad (19)$$

while  $A = \gamma$  and  $B = g$  corresponds to the shear-clustering cross-correlation. Note that the galaxy bias,  $b_{\text{gal}}$ , will in general be different from that of the galaxies in the spectroscopic sample discussed in Sect. 2.1. Moreover, as mentioned in this subsection, the (binned) redshift probability distribution of sources,  $n_i(z)$ , used for clustering might differ from that employed for cosmic shear.

A combined analysis including all of such correlations is commonly referred to as a ‘ $3 \times 2$ pt analysis’. It can significantly enhance the constraining power: for *Euclid* the FoM is increased by roughly a factor 20, relative to a cosmic-shear-only scenario (Tutusaus et al. 2020; Euclid Collaboration: Blanchard et al. 2020). Hence, it should not come as a surprise that such an approach has become the standard for current surveys (e.g. van Uitert et al. 2018; Joudaki et al. 2018; Abbott et al. 2018a, 2022; More et al. 2023). Additional cross-correlations, for instance with CMB measurements (Sect. 9.4), can be included for  $n \times 2$ pt analyses (e.g. Abbott et al. 2019, 2023).

The benefit of combining these three types of correlations lies in their ability to lift degeneracies between parameters (both cosmological and nuisance), such as the galaxy bias parameters that are needed to describe how galaxies trace the underlying

matter distribution. In contrast, galaxy clustering is not affected by intrinsic-alignment and shape-measurement biases. Moreover, the clustering-shear cross-correlation is subject to the same systematic effects as cosmic shear and galaxy clustering, but has a different functional dependence. Combining these probes allows for the partial self-calibration of systematic effects (Bernstein & Jain 2004; Hu & Jain 2004; Bernstein 2009; Joachimi & Bridle 2010). This self-calibration enables tight control over systematic effects. Thus, the main cosmic shear cosmological results from *Euclid* will be derived from a  $3 \times 2$ pt analysis, made possible by the precise weak lensing measurements. In the cosmological parameter forecasts in Sect. 8.2.3, we present the expected parameter constraints from this analysis.

The improved constraining power comes at a price: we need to accurately measure and consistently model a larger number of probes. In principle, photometric clustering includes all the physical effects described in Sect. 2.1, including BAOs and RSDs. However, given the lack of resolution along the LoS, the information is generally projected within each tomographic bin, similar to what is done for weak lensing. By limiting the analysis to the angular correlation function between galaxies, most of the RSD signal is lost (although not completely, see Euclid Collaboration: Camera et al., in prep.). However, we need to include RSDs in the modelling in order not to bias our cosmological results (e.g. Euclid Collaboration: Tanidis et al. 2024).

Moreover, thanks to the low radial resolution of this probe, the BAO signal is partially smoothed out and therefore we can use smaller scales than those considered in spectroscopic clustering analyses, even if our model is not as accurate. As a result, most of the information from photometric galaxy clustering comes from scales slightly smaller than those used in Sect. 2.1, making them complementary probes. We note, however, that photometric galaxy clustering still uses biased tracers; therefore, we cannot use scales as small as for weak lensing, given the difficulty in modelling the galaxy bias at small scales. Another physical effect that needs to be included in the modelling of the signal is magnification. This lensing effect does not add much constraining power (Mahony et al. 2022), but ignoring its impact on the clustering signal leads to biased parameter estimates (see e.g. Duncan et al. 2022; Euclid Collaboration: Lepori et al. 2022; Martinelli et al. 2022). For galaxy-galaxy lensing, all these effects also need to be considered, in addition to those relevant for weak lensing.

A robust measurement of photometric clustering poses new challenges, in part owing to its reliance on ground-based data that were obtained under varying observing conditions. If these variations are not accounted for, they can lead to spurious clustering (Ross et al. 2011; Elvin-Poole et al. 2018; Johnston et al. 2021; Rodríguez-Monroy et al. 2022). Further complications arise from contamination by stars and Galactic extinction, or zodiacal light, which can change the galaxy counts on relatively large scales. In principle, these contributions are included in the visibility mask (see Sect. 7.7.2), which is used to correct the measurements. Work to optimise the galaxy samples is ongoing. In particular, it may be advantageous to consider samples of bright galaxies, which are more immune against spurious clustering.

## 3. Spacecraft and instruments

The primary cosmological probes of *Euclid*’s core science case have defined the main survey characteristics (Sect. 4), as well as the requirements for the capabilities of the telescope and instrument. Besides a maximum cost, in accordance with its ‘medium’ mission size, ESA imposed a so-called technology readiness

level of 5 or higher for the components of the proposed mission. This restriction allows only the use of technologies that have already been validated in the relevant environment.

Before *Euclid*'s final design and scope were defined, initial assessment studies with industry and the science community resulted in a set of feasible science and mission requirements. The subsequent definition phase provided a detailed description of the scientific scope based on a mission design that could be developed within the programmatic constraints set by ESA (Laureijs et al. 2011). After its selection in 2011, the *Euclid* mission was adopted by ESA's science programme committee in June 2012, to enter the implementation phase with industrial contracts for the development of the space segment and with a multilateral agreement between ESA and the participating countries for the delivery of the two science instruments and the development of the science ground segment.

*Euclid* was originally planned to be launched on a Soyuz ST-2.1B rocket (Laureijs et al. 2011), but the geopolitical developments that unfolded in 2022 resulted in the cancellation of this possibility. Investigations revealed that a SpaceX Falcon-9 could provide a suitable alternative, which was ultimately confirmed with the successful launch on 1 July 2023 into an orbit around the second Lagrange point of the Sun-Earth system (hereafter L2). This orbit provides a thermally stable environment with unobstructed views of the sky, prerequisites for a successful use of the planned cosmological probes. The most salient details about the spacecraft are presented in Sect. 3.1. Information about the transfer into the halo orbit around L2 and orbital maintenance is provided in Sect. 3.2, while pointing constraints are discussed in Sect. 3.3.

The spacecraft contains two main science instruments: the visible imaging instrument (VIS; Sect. 3.4); and the Near Infrared Spectrometer and Photometer (NISP; Sect. 3.5). Both instruments were designed to provide high-quality data over a wide field of view (FoV) with a high degree of accuracy and precision. The resulting homogeneous, high-quality space-based observations benefit from the thermally very stable environment, and from the absence of atmospheric blurring and bright sky background, providing a data set of unrivalled fidelity.

### 3.1. Spacecraft

The *Euclid* spacecraft can be subdivided into three main parts: the service module (SVM); the payload module (PLM) including the telescope; and the scientific instruments (called collectively 'extended PLM'). The design of the spacecraft is described in detail by Racca et al. (2016); here, we present a summary overview and the most important changes until launch, and observations during the commissioning phase.

#### 3.1.1. Service module

The SVM comprises the spacecraft subsystems supporting the payload operations; it hosts the warm electronics of the payload, and provides structural interfaces to the PLM and the launch vehicle. The prominent sunshield is part of the SVM. It protects the PLM from illumination by the Sun and supports the photovoltaic assembly supplying electrical power to the spacecraft. On top of it, a triple blade sun-baffle is mounted with the purpose to reduce the sunlight diffracted towards the PLM baffle aperture. The overall spacecraft envelope fits within a diameter of 3.74 m and a height of 4.8 m. *Euclid*'s total launch mass budget, including propellant for operations, is 1988.1 kg (see Table 2). The left panel in Fig. 5 shows an overview sketch of *Euclid* in launch

**Table 2.** System mass budget for launch.

| Component                                       | Mass (kg)        |
|-------------------------------------------------|------------------|
| Service module (SVM)<br>(Warm instrument units) | 901.0<br>(64.5)  |
| Payload module (PLM)<br>(Cold instrument units) | 806.4<br>(156.4) |
| Propellant ( $N_2H_4$ and $N_2$ )               | 210.7            |
| Launch vehicle adaptor and clamp band           | 70.0             |
| Total launch mass                               | 1988.1           |

**Notes.** The SVM and the PLM masses include the instrument units located in each module, reported below each item.

configuration, including the definition of its axes, while the right panel shows the fully assembled spacecraft during testing in February 2023.

#### 3.1.2. Payload module

The *Euclid* PLM is designed around a three-mirror anastigmat Korsch telescope (Korsch 1977) with a 1.2-m primary mirror and an effective collecting area of 0.9926 m<sup>2</sup> (Gaspar Venancio et al. 2014). The telescope provides a common area between instruments of about 0.54 deg<sup>2</sup> with minimal spherical aberration, astigmatism, coma, and field curvature. The mirrors and telescope structure are made from silicon carbide (SiC; Bougoin et al. 2019), with the optical path schematically shown in Fig. 6. The light separation between the two instruments is performed by a dichroic plate located at the exit pupil of the telescope. The PLM provides the mechanical and thermal interfaces to the instruments, consisting of radiating areas and heating lines.

Whereas NISP is a stand-alone instrument with interface bipods, VIS is delivered in several separate parts. It consists of a focal plane assembly (FPA) containing all detectors, connected to proximity electronics, readout shutter unit, and calibration unit, each with their own dedicated mechanical and thermal interfaces with the PLM.

The secondary mirror (M2) is mounted on the M2 mechanism (M2M), allowing adjustment in three degrees of freedom for focusing and some optical alignment. In addition, the PLM hosts the fine-guidance sensors (FGSs), used as pointing reference by the attitude and orbit-control system (AOCS). The FGS detectors are mounted on the same structure carrying the VIS focal plane to ensure precise co-alignment. Except for the proximity electronics of the VIS and FGS focal planes, all electronics are placed on the SVM to minimise thermal disturbances of the PLM.

The PLM is divided into two cavities, separated by the baseplate. The front cavity includes the primary and secondary mirrors of the telescope, as well as the M2M and the associated support structure. This cavity is thermally insulated by a baffle that functions as a stray light shield and as a thermal radiator at the same time. Figure 7 shows an annotated overview of the instrument cavity, which includes the telescope folding mirrors, the tertiary mirror M3, the dichroic plate, the FGS, and the two instruments NISP and VIS – the latter with its separate FPA, filter and grism wheels, and calibration source components.

The PLM's mechanical architecture is based on a common SiC baseplate that supports on one side M1 and M2, and on the

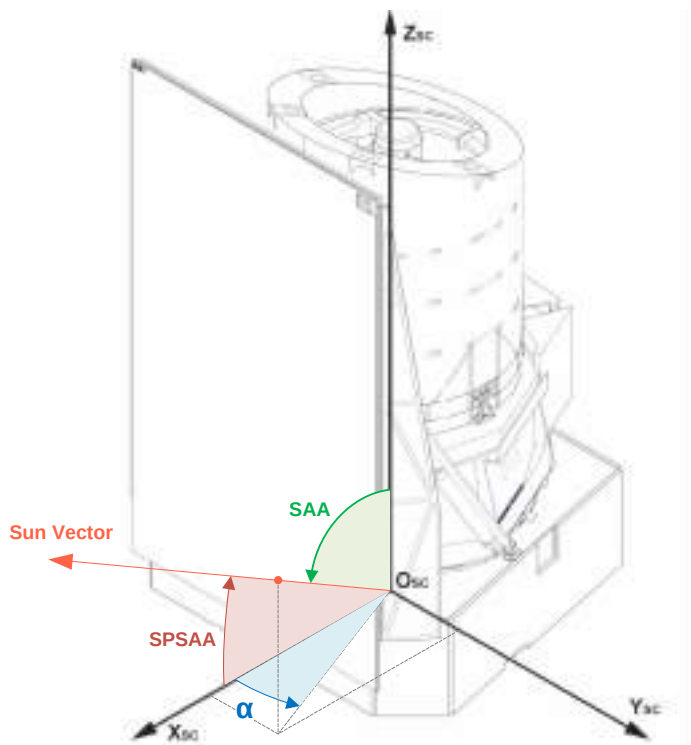


**Fig. 5.** *Left:* Overview of the *Euclid* spacecraft with the principal axes highlighted. *Right:* The fully assembled spacecraft on February 2023 in the anechoic chamber of Thales Alenia Space in France, after completing final electromagnetic compatibility tests. The side shown here will always face away from the Sun. The large white structure below the cylindrical telescope baffle is the NISP radiator. The hydrazine thrusters still have their protective red covers on. The plaque with the miniaturised fingerprint galaxy created thanks to a [collaboration with visual artist Lisa Pettibone](#) and Euclid Consortium members can be seen at the lower left. Figure credit: ESA – M. Pédoussaut.

other side the remaining optics and the two instruments. On the baseplate two planar low-pass coated folding mirrors, FoM1 and FoM2, fold the optical beam in the plane of the baseplate at the entrance of the instrument cavity between M2 and M3. A third, silver-coated folding mirror (FoM3) allows us to have the VIS instrument close to a radiator to efficiently remove the front-end electronics' heat. The telescope is cooled down to its equilibrium temperature (M1 temperature around 126 K). This cold telescope offers high thermo-elastic stability, where the SiC's coefficient of thermal expansion is reduced to  $0.4 \mu\text{m m}^{-1} \text{K}^{-1}$ , and provides a time-stable cold environment for the instruments. The baseplate temperature range of 130 K to 135 K is maintained constant during the mission to about 200 mK and to a few tens of millikelvin during the observations. The main drivers of the baseplate temperature are the attitude of the spacecraft and the local heat dissipation generated by the instrument units operational status.

### 3.2. Transfer and orbital maintenance

*Euclid* operates from a large-amplitude quasi-periodic halo orbit around L2, with a maximum Sun-Spacecraft-Earth angle of  $35^\circ$  and a period of about half a year. *Euclid* travelled on a so-called stable manifold towards its operational orbit, which did not require an orbit-injection manoeuvre. The Falcon-9 launch vehicle injected *Euclid* very accurately to this stable manifold. Of the three planned transfer correction manoeuvres (TCMs), only two were required. The first one was executed one day into the mission, providing a  $\Delta v = 2.14 \text{ m s}^{-1}$  to remove the

launcher dispersion. The second TCM, three weeks after launch, delivered a correction of  $\Delta v = 0.19 \text{ m s}^{-1}$ . Overall, a total of  $\Delta v = 50 \text{ m s}^{-1}$  was budgeted for all three TCMs, meaning that a considerable amount of propellant (about 43 kg) was saved for the scientific mission. However, it should be pointed out that the amount of hydrazine propellant is not a sizing parameter for the mission duration, which is limited by the amount of gaseous nitrogen used by the micro-propulsion system during the science observations.

The launch day and lift-off times were selected such that the resulting operational orbit is eclipse-free, without excursions into the Earth and Moon shadows. Such an excursion would result in a considerable thermal disturbance and also power limitation. The quasi-periodic halo orbit around L2 is dynamically unstable, that is the perturbations grow exponentially over time. Perturbations can be non-gravitational, from sources such as out-gassing ([Euclid Collaboration: Schirmer et al. 2023](#)), imperfect thruster firings, leakage, variable solar radiation pressure, and offloading of wheel movements. Further perturbations occur in the time span from the on-ground processing to the actual correction manoeuvre; that is, the latter does not perfectly fit the true orbit anymore. The time constant of the exponential decay of a typical wide halo orbit is 22–23 days, and escape from the operational orbit occurs after approximately 90 days.

Station-keeping or orbital maintenance is achieved by thruster firings on a regular basis. A more frequent orbital maintenance keeps the exponentially growing perturbations better in check, meaning a smaller total velocity correction  $\Delta v$  needs to be applied each year, saving propellant. *Euclid* requires slots of

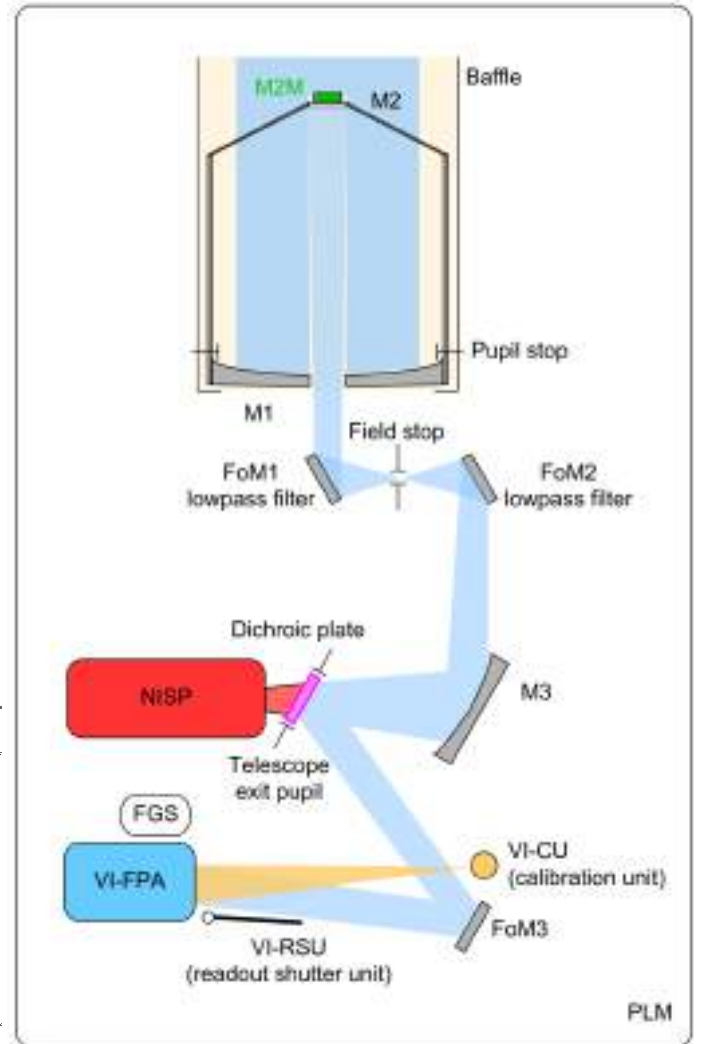
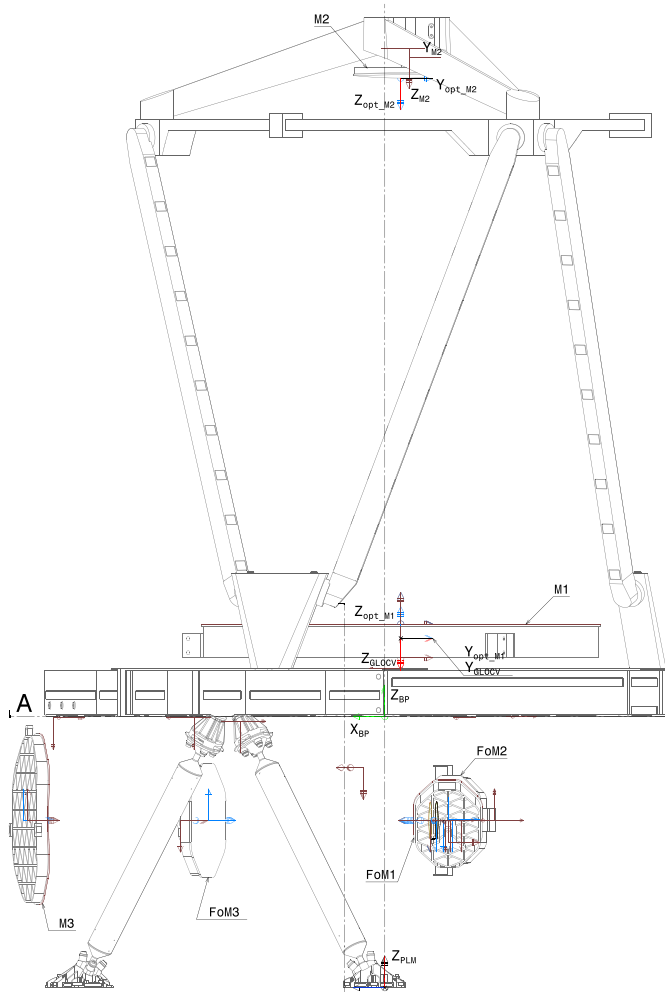


**Fig. 6.** *Left:* Technical layout drawing of the PLM optical surfaces to scale. Note that the dichroic plate and the field stop are not shown as covered by the FoM1 in this view. *Right:* Schematic functional view: light enters from the top onto the primary mirror M1. The secondary mirror M2 can be moved in 3 degrees of freedom by the M2M to compensate launch and cool-down effects. Separated by a baffle, the light then enters the instrument cavity, where it gets relayed by two flat folding mirrors (FoM1, FoM2) whose coatings suppress photons below  $0.5 \mu\text{m}$ . The tertiary mirror M3 directs the beam towards the dichroic plate. In transmission light enters NISP and in reflection VIS, by use of a third folding mirror (FoM3, silver coated). VIS consists of a separate FPA, an RSU, and a CU. *Euclid's* FGS are co-mounted on the same structure as the VIS FPA. Figure credit: ADS.

about 6 h per orbital maintenance, which would considerably reduce the time available for the survey if executed too frequently. The best compromise between propellant efficiency and survey efficiency for *Euclid* is by scheduling orbital maintenance at fixed intervals of 28 days (see also [Euclid Collaboration: Scaramella et al. 2022](#)). A total of 1000 orbital years were simulated by ESA, assuming various cases of residual acceleration from non-gravitational factors, spanning from  $1 \times 10^{-9} \text{ m s}^{-2}$  to  $6 \times 10^{-8} \text{ m s}^{-2}$ . The yearly required  $\Delta v$  with a 28-day maintenance schedule then ranges between  $0.76 \text{ m s}^{-1}$  and  $7.00 \text{ m s}^{-1}$ , dependent on the assumed expected stochastic residual acceleration of the spacecraft. Other ESA missions at L2, such as *Gaia*, *Planck*, and *Herschel*, were found to be in this range of acceleration in their respective orbit-assessment analyses.

At the time of writing, only a few orbital maintenance manoeuvres were executed, insufficient to make a reliable estimate of the actual long-term fuel consumption. The current budgeting for *Euclid* is therefore necessarily conservative and for the worst case  $\Delta v = 7 \text{ m s}^{-1}$  per year assuming corrections

every 28 days. These burns would last about 50 s on average and consume approximately 1 kg of hydrazine propellant. *Euclid* carries a total of 137.5 kg of hydrazine for transfer corrections into the L2 orbit, orbit maintenance for six years, and disposal into a heliocentric graveyard orbit ([Racca et al. 2016](#)). The latter is required by ESA's space-debris mitigation code of conduct, and requires up to  $\Delta v = 10 \text{ m s}^{-1}$ .

### 3.3. Pointing constraints and data downlink

The *Euclid* image quality requirements demand very precise pointing stability, while the survey requirements call for fast and accurate slews. The image quality requirements were translated into AOCS requirements on the relative and absolute pointing errors (RPE and APE, respectively) at the 99.7% confidence level. In science mode, the allowed RPE over a period of 700 seconds<sup>11</sup> around the X- and Y-axes of the spacecraft is 75 mas

<sup>11</sup> The longest *Euclid* science exposures are about 570 s (see Table 3).

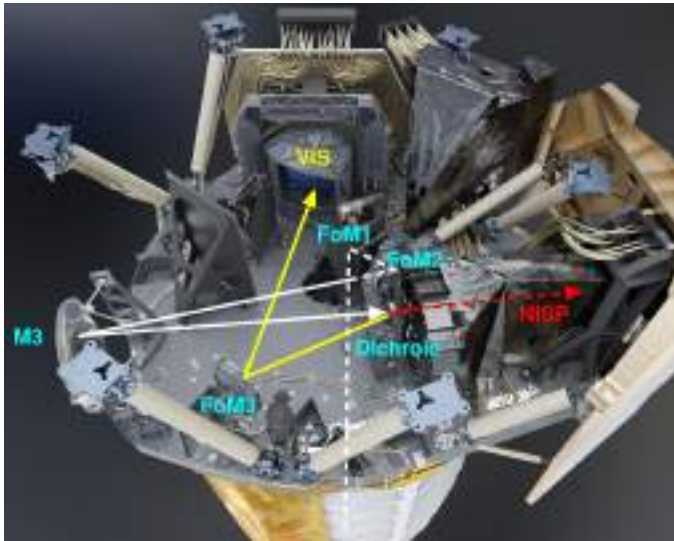


**Fig. 7.** 3D digital rendering of the instrument cavity. In this orientation the telescope is below the assembly and observing towards the bottom. For clarity, we have added the principal light path and optical components to the rendering; dashed lines are obstructed from the chosen point of view. The large structure to the right of NISP is its outward-facing radiator. It can be clearly seen in the photograph shown in Fig. 5. Figure credit: ADS, annotations by the authors.

(milli-arcseconds), and  $1''.5$  around the Z-axis (roll angle). The allowed APE is  $7''.5$  around the X- and Y-axes, and  $22''.5$  around the Z-axis.

An FGS with four charge-coupled device (CCD) sensors co-located within the focal plane of the telescope at the side of the VIS imager provides the fine attitude measurement based on a pair of operational CCDs. Cold-gas micro-propulsion thrusters with micro-Newton resolution provide the fine torque commands used to achieve the high-accuracy pointing. The gyro- and FGS-based attitude control corrects for low-frequency noise, ensuring that the RPE requirement is met. Three star tracker optical heads used in a 3:2 cold redundancy scheme provide the inertial attitude. The star trackers are mounted on the SVM and are thus subject to thermo-elastic deformation when large slews are executed. The FGS is also endowed with absolute pointing capabilities – based on a reference star catalogue – to comply with the APE requirement. This capability allows the autonomous cross-calibration of the star trackers and FGS so that the commanded target attitude is achieved for the subsequent observation. A high-performance gyroscope is included to propagate the FGS attitude between two measurements and during the temporary FGS outages, for example, when operating the VIS shutter (see Sect. 3.4 below).

Three or four reaction wheels execute the science mode slews, specifically field, dither, and large slews between different sky zones. Before the end of the slew manoeuvre, the wheels' torques are commanded to zero and the wheels are left to brake on their own friction. Keeping the reaction wheels at rest during observations ensures noise-free science exposures by eliminating micro-vibrations and torque-noise effects.

Finally, to optimise the PSF (Sect. 7.6.4) and reduce its variability, thermal variations need to be minimised to avoid degrading the image quality as much as possible. This places restrictions on the spacecraft attitude and internal power dissipation variations that can be tolerated. To quantify these, an analysis of the full structural thermal optical performance

(STOP) of the satellite was performed, where the impact of the spacecraft attitude variations on the PSF stability was studied (Anselmi et al., in prep.). This resulted in limiting the allowed range in Solar aspect angle (SAA) and alpha angle (AA). SAA is defined as the angle between the spacecraft's Z-axis (telescope pointing direction; see Fig. 5) and the Sun vector (direction to the centre of the solar disk from the origin of the spacecraft reference frame). AA is defined as the angle between the Sun vector projected onto the X–Y plane and the X-axis, and it increases as the spacecraft rotates clockwise about its +Z-axis. In addition to the range limitation, further minimisation of the field-to-field variation in these angles is desirable. The range of AA and SAA considered and its implication for the survey design are discussed in Sects. 4.1 and 5.4.

### 3.3.1. Data downlink

*Euclid* can use a 4-hour long daily telemetry communication period (DTCP) to downlink its science data and recorded telemetry, about 826 Gbit of compressed data per day, either to the Cebreros (Spain) or the Malargüe (Argentina) ground station. The science data are transmitted using the consultative committee for space data systems file delivery protocol (CFDP), which simplifies science operations and processing. This is the first time this protocol has been used from L2. The downlink is performed with *Euclid*'s steerable 70-cm diameter K-band high-gain antenna (HGA). From *Euclid*'s perspective, the Earth traces approximately a wide ellipse on the sky every 6 months, with an opening angle of about  $35^\circ$  and the Sun near the centre. The beam width of the HGA is smaller than the apparent diameter of the Earth as seen from *Euclid*, about  $0''.5$ , meaning that the HGA's position must be adjusted frequently. Adjustments are permitted during spacecraft slews only, so as not to disturb the pointing stability during an ongoing observation.

Within a DTCP window the HGA follows a ground station, accounting for Earth's rotation for maximum antenna gain. The HGA is repositioned with every dither slew, that is 3 times per survey field or approximately every 20 minutes. Outside a DTCP window the HGA is repositioned to the position where a ground station is expected to appear at the next DTCP. This happens every 72 min when slewing to the next survey field, but an actual antenna movement might not be required every time.

To simplify spacecraft operations, the DTCP windows are decoupled from the scientific observations, that is the HGA must be allowed to reposition at most every 50 minutes. This means that *Euclid* cannot stare at the same position on the sky for longer than 50 min. Both the *Euclid* survey and our calibration programme (Sect. 4.3) are designed to fit within this constraint, which will likely also apply to future mission extensions and potential mini-surveys during windows of unallocated time (Sect. 4.1.2).

### 3.3.2. Pointing accuracy and stability

In-flight estimates of the absolute pointing error (APE) are larger than the requirements by a factor 2 or more:  $3''.5$  around the spacecraft's X-axis,  $2''.8$  around the Y-axis, and  $7''$  around the Z-axis, with the axes shown in Fig. 5. This is sufficient for survey purposes, but it also means that *Euclid* cannot place an object onto a specific pixel.

Similarly, the RPEs can be estimated from a range of orbital house-keeping parameters, providing slightly different results as they were intended for different purposes. We used the RPE contained in the AOCS 'guidance error' vector and the absolute

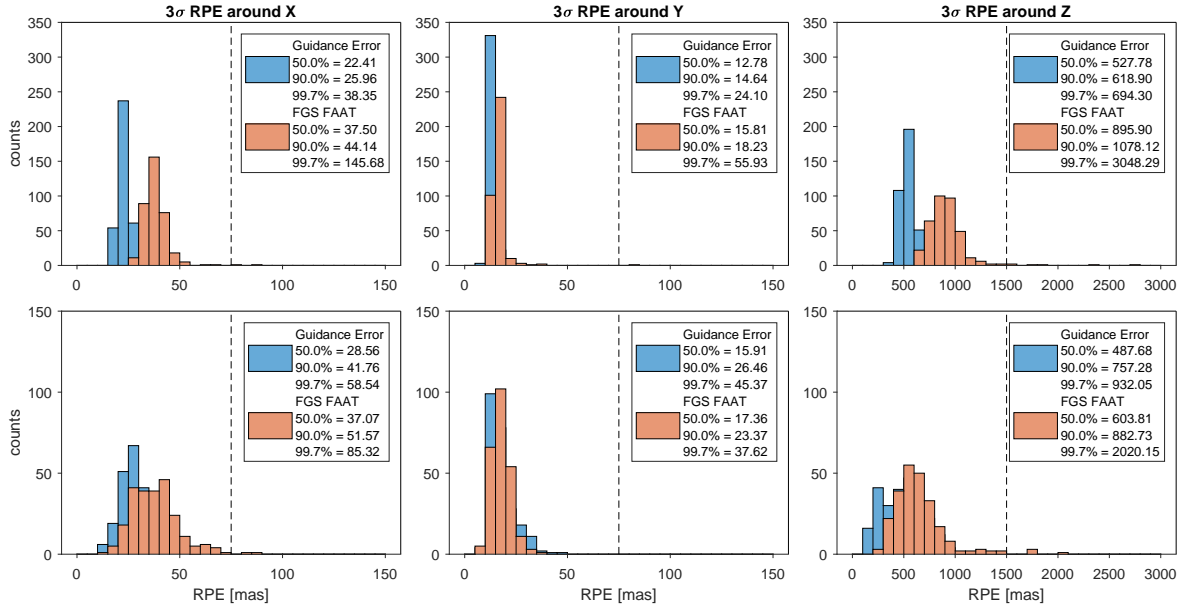


**Fig. 8.** RPE performance in 360 nominal (*top row*) and 243 short (*bottom row*) VIS science exposures. The blue histograms are based on the AOCS controller-error vector, and the orange ones on the FGS-provided absolute quaternion. The dashed vertical lines show the  $3\sigma$  allocation by industry. Even though that requirement is not always met in practice, in particular about the  $z$ -axis, it does not mean that the PSF requirements are violated, because there are also margins on the optical PSF.

quaternion produced by the FGS. In Fig. 8 we show our findings from an analysis of 360 VIS nominal science exposures and 243 VIS short science exposures taken from 5 to 9 December 2023, after an AOCS software update to improve the pointing performance. These results should be representative for the remainder of the survey.

Accordingly, for nominal exposures the RPE around the  $X$ -axis is poorer than around the  $Y$ -axis, but still fully compliant if the guidance error vector is considered (38 mas at 99.7% confidence level), while it would exceed the requirement (75 mas) if the FGS absolute quaternion is considered. Around the  $Y$ -axis the requirements are fulfilled using both indicators. Around the  $Z$ -axis the situation is similar to the  $X$ -axis and the requirement (1500 mas) is exceeded if the FGS absolute quaternion is considered. The RPE for short science exposures is somewhat different due to the larger fraction of the stabilisation time in the exposure. A full discussion of these results is beyond the scope of this paper. Concerning the PSF reconstruction, the FGS absolute quaternion should be used only for the  $X$ - and  $Y$ -axes, while for the  $Z$ -axis the pointing derived from the FGS quaternion should be combined with the more accurate gyroscope vector.

The pointing stability during an exposure is about 35 mas or  $1/3$  of a VIS pixel around the  $X$ - and  $Y$ -axes with 99.7% confidence. This is achieved by continuous operation of cold-gas thrusters to counter non-gravitational accelerations, mainly from solar radiation pressure but also from outgassing. In the magnitude range 10 to 19, *Euclid*'s FGS can find sufficient guide stars for the great majority of fields ( $\geq 99.9\%$ ) when the telescope is focused; exceptions are *Euclid*'s VIS wavefront-retrieval observations, where the telescope must be slightly defocused (Sect. 4.3.2).

### 3.4. Visible instrument: VIS

To enable the weak gravitational lensing science discussed in Sect. 2.2, accurate shapes need to be measured for about

1.5 billion galaxies. This requires an instrument that can image large parts of the Universe with fine spatial resolution. Galaxies in the redshift range  $0.2 < z < 2.5$ , which will be used to map dark matter, have typical angular diameters of  $0''.3$  and must be sampled with  $0''.1$  resolution or better. The *Euclid* instrument designed to meet these requirements, VIS, is a large-format imager with an FoV of  $0.54 \text{ deg}^2$  sampled at  $0''.1 \text{ pixel}^{-1}$ , operating in a single red passband. The considerations driving the VIS design, and its development and initial performance, are described in detail in *Euclid Collaboration: Cropper et al. (2025)*; a brief overview is provided here. A mosaic of the VIS subsystems is shown in Fig. 9.

The cosmological lensing signal is extracted from a statistical analysis of a large number of coarsely sampled faint galaxies. With sample sizes to achieve the precision targeted in Sect. 2.2, biases in the measurements become dominant. Obtaining meaningful results, therefore, depends critically on a deep understanding of the instrumental effects. VIS fits within a system of external optics, calibrations, and survey design, all of which have been highly and mutually optimised to meet the stringent performance required for weak gravitational lensing (Cropper et al. 2013). VIS is therefore designed to be maximally stable and able to be calibrated.

The VIS detectors are CCDs, which were chosen because of the detailed understanding gained from past missions on their behaviour and performance in the space environment, and their stability, which results from the signals passing through a limited number of readout nodes. In order to cover the large FoV, VIS has 36 CCD273-82 designed and manufactured by e2v (Endicott et al. 2012) to a custom *Euclid* specification (Short et al. 2014) in a  $6 \times 6$  array (see Fig. 10). Each CCD has  $4132 \times 4096$  pixels in four quadrants, so the VIS images comprise  $6.09 \times 10^8$  pixels. The pixels in the 144 separate quadrants are read out synchronously, to minimise noise, and digitised to 16-bit precision by 12 front-end electronics units. They are then passed to a control and data processing unit (CDPU; Di Giorgio et al. 2010, 2012;



**Fig. 9.** Constituents of VIS. *Top:* The VIS focal plane showing (from left to right) the array of 36 close-butt CCDs within their SiC structure, as integrated on the PLM; a ‘slice’ of six CCDs with a pair of ROEs to control them and digitise the signals; and the integrated focal plane with a protective cover for the CCDs (six power supplies for each ROE can be seen on the left of the structure with the other six out of view behind it). *Bottom:* From left to right: the CU used for providing a flat illumination of the focal plane at six different wavelengths; the shutter; the Control and Data Processing Unit, which controls the instrument, sequences the 144 channels of data from the 36 CCDs, compresses the image, and communicates with the spacecraft; and the Power and Mechanism Control Unit, which drives the shutter and the CU. All of these have redundant halves except for the multiplexers on the CDPU to the 12 ROEs.

Galli et al. 2014), where the image is constructed and losslessly compressed, then sent to the spacecraft for downlink to Earth.

The CCDs are held in an SiC structure (Martignac et al. 2014) within the PLM at 153 K to minimise dark noise and optimise their performance in the presence of radiation damage (mainly by solar protons) to the Si-lattice within the devices. Although the pixel-to-pixel transfer of charge during readout of the image is very good, electrons can be temporarily trapped if they encounter a damaged site. When they escape, they can then be released into a charge packet of a later pixel. Hence galaxy shapes can be distorted because of missing charge in their pixels closer to the readout register or readout node, and spurious additional charge in pixels further from them. These distortions have a direct effect on the measured shape of a galaxy and are therefore of concern (e.g. Massey et al. 2014; Israel et al. 2015). A number of enhancements to minimise these effects were incorporated into the *Euclid* CCD273-82 design, including an enhanced capability to inject charge directly into the image area, even at low charge levels, to quantify the distortions from the traps. Its operational parameters were optimised for *Euclid* in an extensive characterisation campaign (Clarke et al. 2012; Prod’homme et al. 2014; Skottfelt et al. 2017b), with novel tri-level clocking schemes and the capability to shuffle charge repeatedly backwards and forwards – referred to as ‘trap pumping’ – to identify trap locations in both the image area and the readout register (Skottfelt et al. 2017a). Charge-injection and trap-pumping calibrations are run repeatedly throughout the survey (see Table 3).

Behind the SiC structure holding the 36 CCDs, 12 sets of readout electronics units (ROEs; Cropper et al. 2016; Szafraniec et al. 2016) set the operating conditions for the CCDs, clock them

**Table 3.** Typical ROS data per survey field.

| VIS                                              |            |
|--------------------------------------------------|------------|
| <b>4 <math>I_E</math>-band nominal exposures</b> | 566 s each |
| <b>2 <math>I_E</math>-band short exposures</b>   | 95 s each  |
| Bias                                             | 2 per day  |
| Dark                                             | 4 per day  |
| Flat                                             | 6 per day  |
| Trap pumping                                     | 6 per day  |
| Charge injection                                 | 8 per day  |
| NISP                                             |            |
| <b>4 red-grism spectro exposures</b>             | 574 s each |
| <b>4 <math>Y_E</math>-band exposures</b>         | 112 s each |
| <b>4 <math>J_E</math>-band exposures</b>         | 112 s each |
| <b>4 <math>H_E</math>-band exposures</b>         | 112 s each |
| 1 Dark                                           | 112 s      |

**Notes.** The total duration of an ROS is 70.2 minutes. About 20 fields are observed per day, cycling through different ROS configurations. While the science exposures (marked with boldface) remain the same, the inline VIS calibrations vary. ROS configurations using the blue grism are used for the *Euclid* Deep Field (EDF) and *Euclid* Auxiliary Fields (EAFs) only. Most NISP calibrations are taken outside the ROS during dedicated calibration blocks.

to read them out and digitise the pixel charge signal from the 144 CCD quadrants. They in turn, with their 12 power supplies, are combined in an aluminium structure (Martignac et al. 2014) that is interfaced to an external radiator to dissipate the heat from the ROEs. These operate at 270 K, so that thermal shields are used

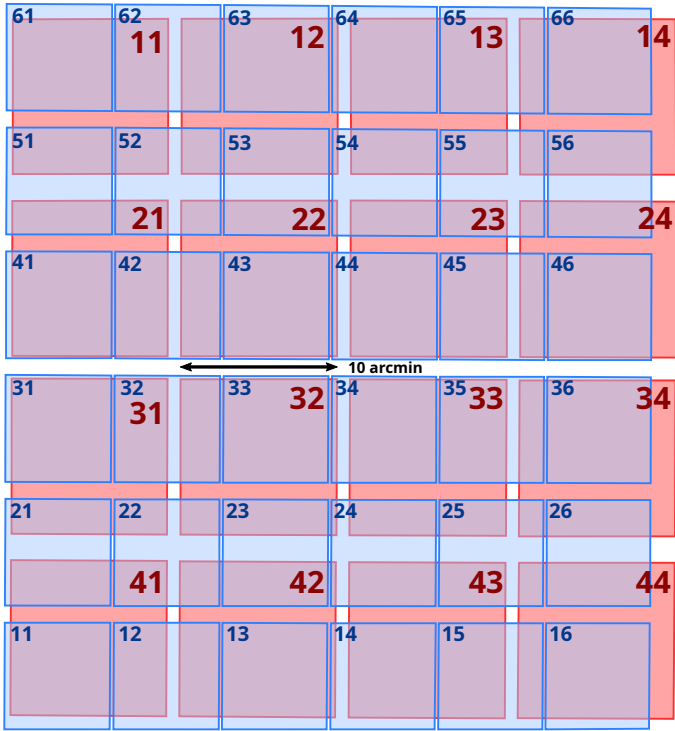


**Fig. 10.** Common instrumental view to the sky of the VIS (blue) and NISP (red) instruments. The footprint was generated from two simultaneously taken VIS and NISP images, astrometrically calibrated and registered to a common pixel grid. Small blue numbers refer to VIS, large red numbers to NISP detector IDs. Interchip gaps are evident. The VIS detectors have an additional thin horizontal gap (not shown here) from the charge-injection lines used to monitor radiation damage through charge-transfer inefficiency. The respective spatial and angular offsets between both instruments are  $52''.5$  and  $0^\circ.078$ .

to minimise the parasitic heating of the CCDs held nearby in their SiC structure, nearly 120 K colder. These two halves comprise the FPA shown in Fig. 9. They are integrated on each side of a substantial SiC bracket on the PLM baseplate (see Fig. 7).

In order to maximise the stability of the VIS imaging, the instrument does not have a filter wheel; at the level required by *Euclid* this would not permit sufficiently repeatable image registration from exposure to exposure. The bandpass  $I_E$  for the instrument is therefore set by the *Euclid* telescope, dichroic plate, the folding optics (Fig. 6), and the quantum efficiency (QE) of the CCDs, to be in the range 530–920 nm, optimised for the spectral energy distribution of the majority of galaxies. The wide band and high throughput (Fig. 11) provide a limiting sensitivity of  $m_{AB} = 26.7$  ( $5\sigma$  point source), so that galaxies with a full width at half maximum (FWHM) of  $0''.3$  and  $m_{AB} = 25.0$  are detected with  $S/N = 10$  in a  $1''.3$  diameter aperture, sufficient for precise shape measurements. At the same time, however, the wide band complicates the shape measurement, because the PSF is chromatic. Although the entire VIS optical channel is in reflection, faint off-axis optical ghosts are created by the rear surface of the dichroic, and these must be masked in post-processing.

The CCDs are read out at 73 kHz to limit readout noise, and require a shutter (Genolet et al. 2016) to avoid image trailing from continuous illumination during readout. For reliability, the shutter is a single leaf with dimensions sufficient to cover the  $343\text{ mm} \times 303\text{ mm}$  CCD array. It is momentum-compensated to a fine degree to minimise the disturbance to the *Euclid*

pointing and hence the recorded PSF, which must be modelled to a high level of fidelity for accurate shape measurements. The shutter and a calibration unit for generating flat fields (Cropper et al. 2018) are driven by a power and mechanism control unit (PMCU; Renaud et al. 2018). This unit and the CDPU reside in the SVM, while the FPA with its electronics, the shutter, and the calibration unit reside in the PLM. The full complement of VIS units is shown in Fig. 9.

### 3.5. Near-Infrared Photometer and Spectrometer: NISP

The second instrument on board *Euclid* is the Near-Infrared Spectrometer and Photometer (NISP, Fig. 12), described in more depth in Maciaszek et al. (2022) and Euclid Collaboration: Jahnke et al. (2025). NISP provides multiband photometry and slitless grism spectroscopy in the wavelength range 920–2020 nm (Fig. 11), using the light transmitted by the dichroic beamsplitter.

#### 3.5.1. Hardware overview

NISP has a common optics and detector system for its photometric and spectroscopic channels, with respective filters and grisms in two wheels<sup>12</sup>. A collimator lens provides for each individual source a nearly parallel beam through the filters and grisms. A subsequent camera-lens assembly, together with slight optical power on grisms and filters, focuses the beam in the detector plane. Details and consequences of this design, such as passband variations, are discussed in Euclid Collaboration: Schirmer et al. (2022).

The filter wheel includes a dark plate that can be used to block all light from the telescope, but not from the calibration lamp, for specific calibration purposes. The lamp uses five nearly monochromatic light-emitting diodes (LEDs) whose wavelengths span the NISP wavelength range to support a wide spectrum of calibrations (Sects. 4.3, 4.3.1 and 4.3.3).

The FPA consists of a  $4 \times 4$  grid of Teledyne Hawaii-2RG (H2RG) detectors with  $2048 \times 2048$  pixels. A four-pixel wide border along the detector edges is not light-sensitive, providing baseline reference pixels for detector monitoring. With a plate scale of  $0''.298\text{ pixel}^{-1}$  and including detector gaps, the NISP FoV covers a nearly square-shaped  $0.57\text{ deg}^2$  (see Fig. 10).

The 16 H2RGs are operated at  $T \approx 95\text{ K}$  to optimise detector behaviour, while the main optics is kept at 130–132 K. Parallel readout occurs in 32 channels per detector using a multi-accumulate (MACC) scheme, with NISP continuously read at a nominal rate of 1.45408 s per frame. For science and calibration exposures, a group of each 16 successive frames is read non-destructively and averaged by the on-board data-processing unit (DPU). Between these groups the exposure just continues and photons are collected, but a number of frames are not read (so-called ‘drops’), either since they would not add up to another group of 16, or due to running into NISP storage limits. At the end, the count rate in each pixel is determined with a linear slope fit to the group values using an iterative algorithm (Kubik et al. 2016). Standard photometry and spectroscopy exposures for the Euclid Wide and Deep Surveys (Sect. 4) use four and 15 groups with 16 frames each, and a number of four and 11 dropped

<sup>12</sup> It is not permitted to use elements from both the filter and grism wheels at the same time, because both have some optical power. Hence, a simultaneous observation through both elements, for example to produce shorter spectra with smaller overlap fractions, results in strongly defocused images.

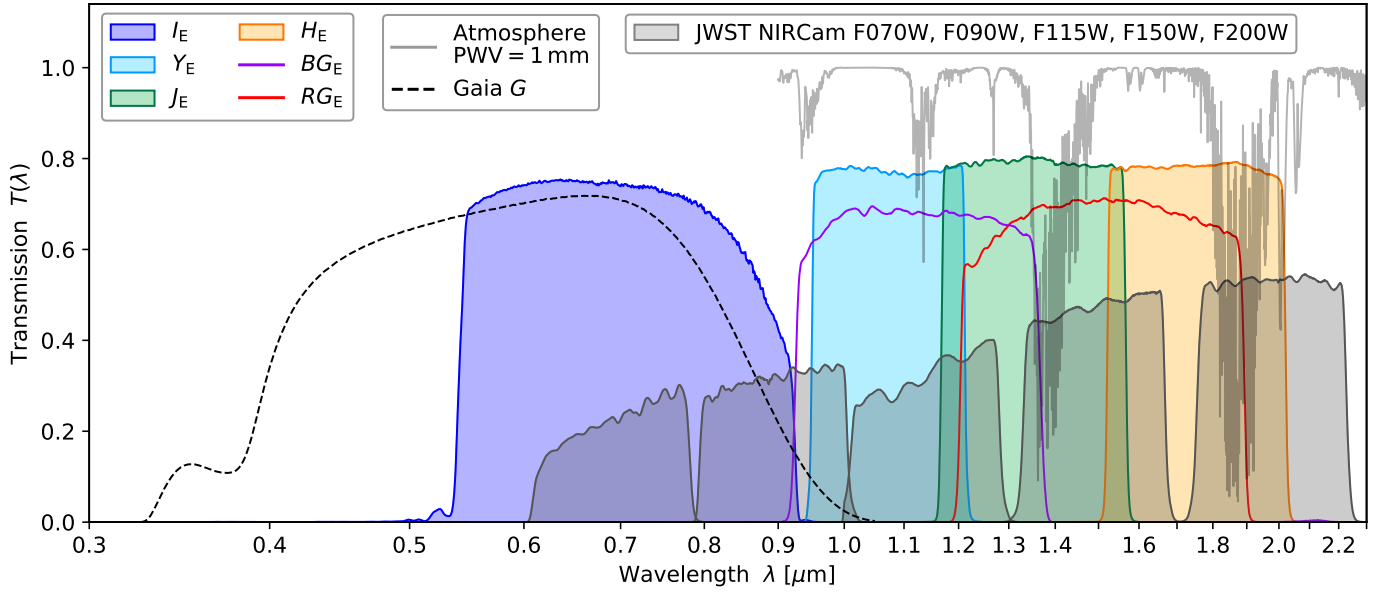


**Fig. 11.** Spectral response of *Euclid*'s imaging (VIS:  $I_E$ ; NISP:  $Y_E$ ,  $J_E$ ,  $H_E$ ) and spectroscopic channels (NISP:  $BG_E$ ,  $RG_E$ ) at the beginning of the mission. The expected transmission loss at the end of the mission due to space weathering and non-volatile contamination is at most 0.05. For reference we show the *Gaia G* passband from their third data release (Gaia Collaboration 2023b), the atmospheric transmission for a precipitable water vapour level of 1.0 mm (Rothman et al. 2013), and some of the JWST passbands of their Near Infrared Camera (NIRCam; Rieke et al. 2005).

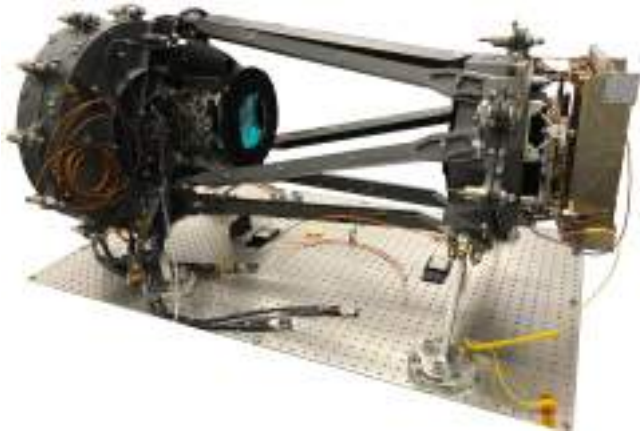


**Fig. 12.** NISP flight model, before wrapping in light-tight multi-layer insulation. Light enters the filter wheel and grism wheel enclosure (left) through a collimator lens, hidden behind the large round wheel enclosure. A triplet camera lens assembly projects the beam onto the cold detector system at the right end of the structure, with the readout electronics to the very right. The NISP calibration lamp is located to the top left of the camera lens assembly in this picture. See Euclid Collaboration: Jahnke et al. (2025) for details.

frames, respectively; we refer to these modes as MACC(4,16,4) and MACC(15,16,11). The effective integration times for the photo- and spectro-exposures are 87.2 s and 549.6 s respectively, while the actual exposure durations are 110.5 s and 572.9 s. The latter times are relevant for the survey planning (Sect. 4), while the former determine the depth of the science data.

NISP uses cold readout electronics at the focal plane, and warm electronics operating at  $T \approx 290$  K located in the SVM. The warm electronics contain both the commanding computer and the DPU. The latter performs the baseline subtraction using reference pixels, the MACC slope fit, and the data

compression. For images the compressed slope-fit image is downlinked together with a 1-bit quality image that encodes whether the slope-fit  $\chi^2$  lies above a certain threshold. For dispersed spectra images the full  $\chi^2$  information is downlinked in an 8-bit quality image. NISP has full redundancy in its warm electronics and calibration-source LEDs, as well as the power supply to drive the filter and grism wheels.

### 3.5.2. Near-infrared imaging

The NISP photometric channel (NISP-P) offers three passbands  $Y_E$  (949.6–1212.3 nm),  $J_E$  (1167.6–1567.0 nm), and  $H_E$  (1521.5–2021.4 nm), displayed in Fig. 11. The wavelengths refer to the 50% peak-transmission points near the centre of the FoV and are accurate to 0.8 nm. Passband variations within the FoV are characterised to  $\lesssim 0.1$  nm. The near-rectangular passband flanks are entirely defined by the 130-mm diameter filters, which carry up to 200 interference coating layers distributed over both filter sides (Euclid Collaboration: Jahnke et al. 2025). The total in-band spectral response, including detectors, is close to 80%. Out-of-band blocking is  $10^{-4}$  or better within 900–2100 nm, and  $10^{-5}$  to  $10^{-7}$  outside this range. These excellent blocking capabilities are jointly achieved by the filters, all other coated optical surfaces in the NISP optical path, and the detectors (Fig. 13). Out-of-band contamination is at most 2.0 mmag for sources with extreme SEDs, and more typically 0.2 mmag. More details about this and the NISP photometric system in general are presented in Euclid Collaboration: Schirmer et al. (2022).

The designed  $5\sigma$  point-source depth of NISP-P for the wide survey is 24.0 AB mag, which we exceed by approximately 0.4 mag (Sect. 5). The plate scale of  $0''.298 \text{ pixel}^{-1}$  considerably undersamples the NISP PSF that has a typical FWHM of 1.10, 1.17, and 1.19 pixel in  $Y_E$ ,  $J_E$ , and  $H_E$  when fitting a Moffat profile (see also Bernstein 2002). The measured PSF size is fully compatible with the on-ground characterisation of the NISP optics (Grupp et al. 2014). Details are given in Sect. 5.

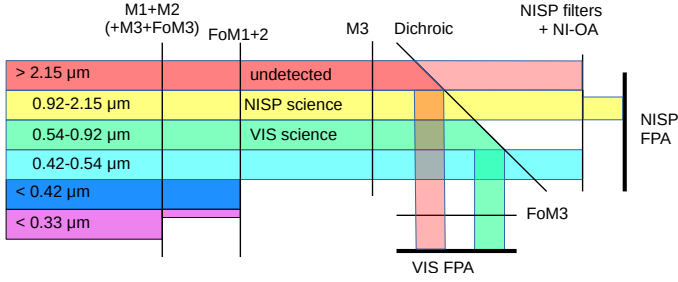


**Fig. 13.** Chromatic selection function of *Euclid*'s optical elements. Since the optical design minimises the number of refractive elements, mirror coatings and the dichroic element play a central role in preparing the passbands for the instruments. The VIS detectors have zero quantum efficiency for  $\lambda > 1.1 \mu\text{m}$ . The behaviour of the dichroic element above  $2.2 \mu\text{m}$  is not specified; longer wavelengths could enter NISP and would be blocked by the filters. Figure adapted from Euclid Collaboration: Schirmer et al. (2022).

### 3.5.3. Near-infrared spectroscopy

The NISP spectroscopic channel (NISP-S) enables the simultaneous acquisition of slitless spectra for thousands of objects across the FoV with uniform quality. The grism wheel houses four different grisms of 140-mm diameter each. The grisms are dispersion gratings combined with a prism whose base is – just like the filters – slightly curved for optimal focus. Dielectric coatings improve out-of-band blocking (Euclid Collaboration: Jahnke et al. 2025). The total spectral response including all optical surfaces and detectors is shown in Fig. 11.

For the spectroscopic observations of the EWS (Sect. 4.1) NISP-S uses three red grisms covering the same  $\text{RG}_E$  passband (1206–1892 nm; 50% peak transmission wavelengths), allowing the detection of  $\text{H}\alpha$  emitters in the range  $z = 0.84$ –1.88. These grisms have different dispersion directions of  $0^\circ$ ,  $180^\circ$ , and  $270^\circ$  with respect to the detector columns. By combining the dispersed slitless images of the same field, overlapping spectra from multiple sources can be disentangled ('decontaminated') and clean spectra extracted. The red grisms have a dispersion of  $1.372 \text{ nm pixel}^{-1}$  and a resolving power of  $\mathcal{R}_{\text{RG}} \gtrsim 480$  for a source with  $0''.5$  diameter. The mission requirement is  $\mathcal{R}_{\text{RG}} > 380$  to achieve a redshift accuracy of  $\sigma(z) < 0.001(1+z)$ . During the ground tests in 2020 it was discovered that the  $270^\circ$  grism does not conform to the specifications and cannot be used for the survey. To achieve spectral decontamination, we use the other two red grisms with additional  $4^\circ$  rotational offsets of the grism wheel, providing a total of four different dispersion directions (for details see Euclid Collaboration: Scaramella et al. 2022). The rotated positions vignette one edge of the detector array by up to 10%, which is accounted for by our calibration, while still meeting the overall image quality requirements.

The designed target sensitivity for the wide survey is a  $3.5 \sigma$  detection for an emission line with flux  $2 \times 10^{-19} \text{ W m}^{-2}$  at 1600 nm (such as redshifted  $\text{H}\alpha$ ), for a source with  $0''.5$  diameter. The in-flight performance was not yet available at the time of writing; however, given the excellent spectral image quality and the fact that NISP-P exceeds its designed depth by 0.4 mag, we are confident that NISP-S also meets its sensitivity requirement.

NISP-S also has a blue grism covering 926–1366 nm, extending the lower  $\text{H}\alpha$  redshift limit to  $z=0.41$ . The blue grism has a resolution of  $1.239 \text{ nm pixel}^{-1}$  and a resolving power of  $\mathcal{R}_{\text{BG}} \gtrsim 400$ . The blue grism is solely used for observations of the *Euclid* Deep and Auxiliary fields (Sect. 4.2). Its main purpose is to provide a large reference sample of galaxies with 99% redshift

completeness and 99% purity required to characterise the typical *Euclid* galaxy population, while maximising the legacy value of these fields (Sect. 10).

## 4. Survey planning

To achieve its primary cosmology objectives, *Euclid* aims to observe a sample of 1.5 billion galaxies for the  $3 \times 2\text{pt}$  analysis, and measure 35 million redshifts for the analysis of the spectroscopic clustering signal. To do so, it needs to cover about  $14\,000 \text{ deg}^2$  of extragalactic sky with low zodiacal background and low Galactic extinction over a period of about six years. In Sect. 4.1 we summarise the design of the EWS. As discussed in Sect. 4.2, these data are complemented by deeper observations over several tens of square degrees, while the performance of the instruments is studied using extensive calibration observations, which are described in Sect. 4.3. Finally, the supporting ground-based observations are summarised in Sect. 4.4 (photometry) and Sect. 4.5 (spectroscopy).

### 4.1. Euclid Wide Survey

Euclid Collaboration: Scaramella et al. (2022) provides a detailed description of the reference EWS. Here, we summarise its characteristics and highlight the main modifications that were implemented prior to launch. The target area has minimal contamination from the Galaxy, Solar System objects, and the zodiacal background, that is the diffuse sunlight scattered by interplanetary dust in the ecliptic plane. The intersection of the avoided regions around the Galactic and ecliptic planes leaves four separate dark areas on the sky for the EWS, which we refer to as the RoI of *Euclid*, indicated by the blue lines in Fig. 14. These areas are adjusted in size to maximise the overlap with the ground-based surveys providing complementary data (Sect. 4.4) needed for PSF modelling and photometric redshift estimation. In the latest pre-launch configuration, the EWS covers  $14\,816 \text{ deg}^2$  of the darkest extragalactic sky, of which  $137 \text{ deg}^2$  are lost due to about 800 bright stars with a magnitude  $m_{\text{AB}} < 4$  in any *Euclid* band. As a result, the effective sky area is  $14\,679 \text{ deg}^2$ .

As detailed in Laureijs et al. (2011), for the VIS imaging we require a  $\text{S/N} \geq 10$  for extended sources with a diameter of 1.2 times the FWHM of the PSF at  $I_E = 24.5 \text{ AB mag}$ . For NISP, we must reach a  $\text{S/N} \geq 5$  for point sources with  $m_{\text{AB}} = 24.0$  in all three NISP bands, and  $\text{S/N} \geq 3.5$  for an  $\text{H}\alpha$  line flux of  $2 \times 10^{-16} \text{ erg cm}^{-2} \text{ s}^{-1}$  at a redshifted wavelength of  $1.6 \mu\text{m}$  in the  $\text{RG}_E$  spectra. We show in Sect. 5 that these depth requirements are met with considerable margin. However, as discussed in more detail in Sect. 5.4, unacceptable levels of stray light were observed for certain spacecraft attitude angles. Avoiding these orientations is possible, but it also means that the effective sky area of  $14\,679 \text{ deg}^2$  for the EWS can no longer be met within the nominal mission duration.

The ROS is the building block of the survey, comprising four dithered exposures that form an 'S'-like pattern; the three dithers that follow the first exposure are in ecliptic coordinates<sup>13</sup>  $(\Delta\alpha, \Delta\beta) = (61'', 111'')$ ,  $(0'', 111'')$  and  $(61'', 111'')$ , respectively. Table 3 lists the data collected during a typical sequence for a given survey field. In addition to the science data, various calibration exposures are obtained. The ROS lasts 70.2 min, followed by a slew to the next adjacent survey field.

<sup>13</sup> In this paper we use the Greek letter  $\alpha$  for the Galactic longitude to avoid confusion with wavelength  $\lambda$ .

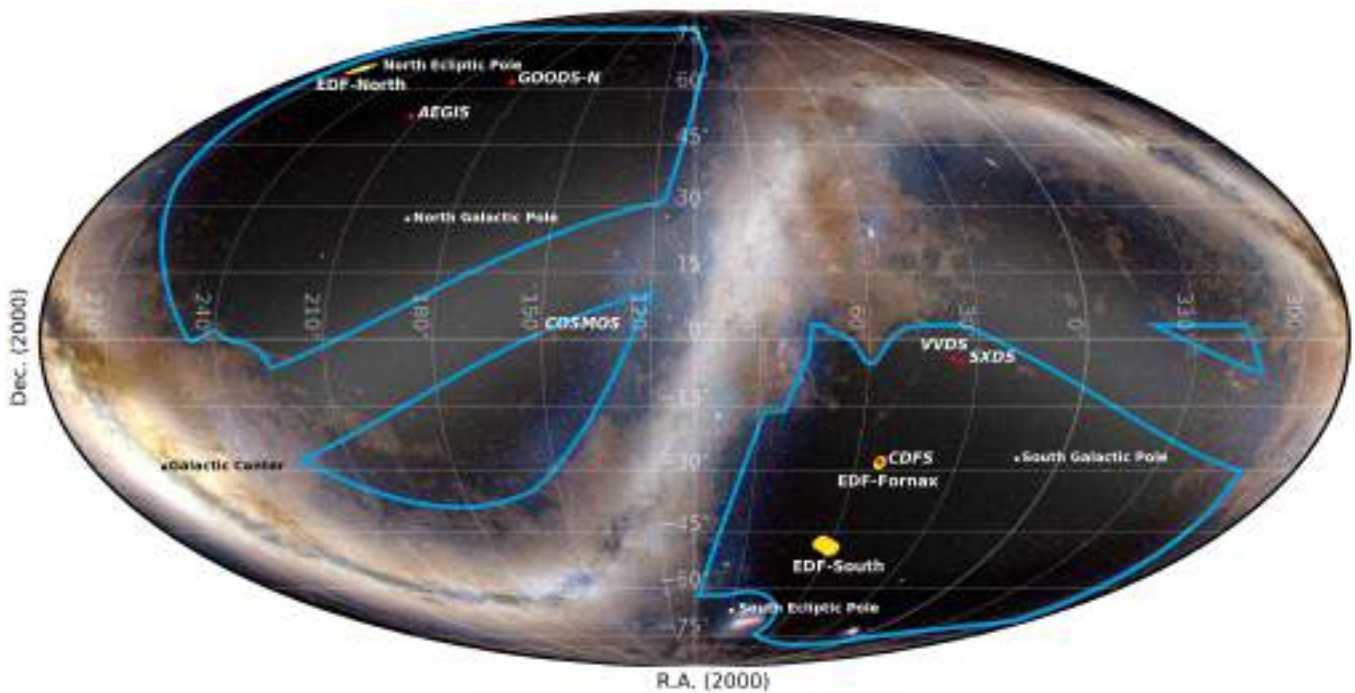


**Fig. 14.** *Euclid* RoI in an all-sky Mollweide projection. The blue borders enclose the  $16\,000\text{ deg}^2$  RoI that contains the observed sky of the *Euclid* Wide Survey. The RoI excludes the Galactic and ecliptic planes. The triangular southern ‘island’ near  $\text{RA} = 330^\circ$  is restricted in size since the LSST does not extend to more northern latitudes. The *Euclid* Deep Fields are shown in yellow and the auxiliary fields with red marks (not to scale).

Such field slews take 2–4 minutes. Occasionally, large slews are required to begin a new survey patch on the sky, or to perform specific calibration observations. These last between 7 and 33 minutes, and their occurrence is kept to a minimum. Hence, about 20 fields are observed per day.

The EWS itself consists of about 27 500 fields, each of which is observed once with the ROS. Including *Euclid* Deep Survey (EDS) and calibration observations, the total survey comprises around 49 000 fields.

#### 4.1.1. Principal survey strategy

Here, we describe the fundamental principles of the survey design. Significant modifications with respect to the pre-launch strategy are introduced in Sect. 5.5, because of the need to avoid stray light that was discovered post-launch at certain spacecraft attitude angles.

For ecliptic latitudes  $-78^\circ < \beta < 78^\circ$  the EWS tessellates the RoI with non-overlapping identical tiles aligned with the ecliptic meridians, distributed along parallels of latitude. This configuration minimises overlaps and maximises survey efficiency. A tile is a FoV placed aligned with the meridian passing through its centre. The size of the tiles is computed from the intersection of the VIS and NISP FoVs. The tiles are observed in a step-and-stare mode by placing the larger *Euclid* common FoV (Fig. 10) on the four dithered positions of each tile. The minimum average overlap between neighbouring fields is 2.2% in area, occurring when all fields are aligned with their respective tiles. For the polar caps at  $|\beta| \geq 78^\circ$  a different tiling strategy was chosen to avoid excessive overlaps due to the converging meridians; details are given in [Euclid Collaboration: Scaramella et al. \(2022\)](#).

The basic position of the *Euclid* spacecraft has its sunshield facing towards the Sun, with the telescope pointing towards the north ecliptic pole (NEP). From this position *Euclid* can rotate

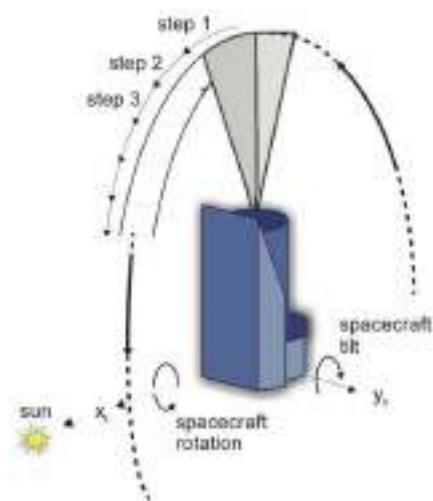


**Fig. 15.** *Euclid*'s main step-and-stare observing mode, showing north-south steps along a circle as rotations around the  $X$ -axis. *Euclid* can tilt to another circle by rotating around the  $Y$ -axis.

freely around the Sun–spacecraft axis, keeping the sunshield orthogonal towards the direction to the Sun, so that it can point to any field on the transit ecliptic meridian,  $90^\circ$  away from the Sun's longitude (Fig. 15). The natural observing mode is to step-and-stare along the transit meridian, effectively sweeping the sky with transit meridians, at an approximate rate of  $1^\circ$  per day, as *Euclid* progresses on its yearly orbit. The full circle defined by a transit meridian is divided in the ‘leading side’, the half-circle pointing in the direction of the spacecraft orbit, and the ‘trailing side’, the opposite half-circle. The two half-circles meet at the ecliptic poles. When observing in the trailing side the FoV is rotated  $180^\circ$  in the sky.

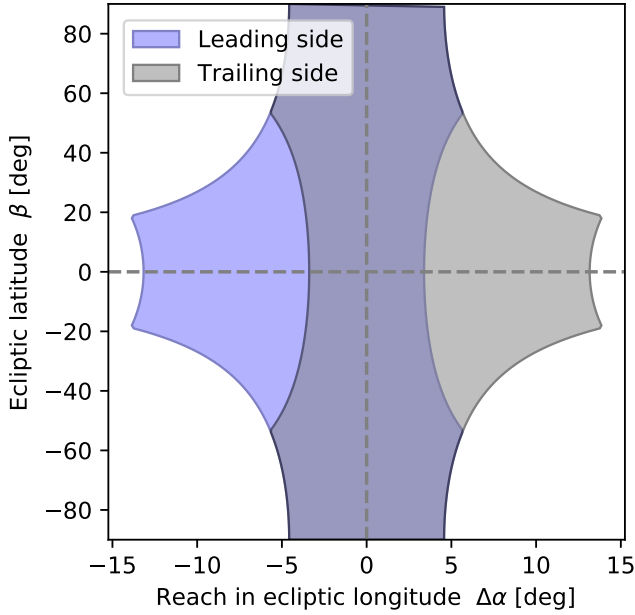


**Fig. 16.** Window of visibility. Shown are the reachable ecliptic longitudes around transit as a function of latitude, computed for  $SAA \in [87^\circ; 104^\circ]$  and  $AA \in [-5^\circ; 5^\circ]$ . A strict tessellation constraint is imposed, meaning the survey fields are not allowed to rotate with respect to the tessellation.

The EWS is frequently halted to observe calibration fields at specific cadences. Moreover, as discussed in Sect. 3.2, all observations must stop every 4 weeks for orbital maintenance. During the interruption, the transit meridian moves and in order for the EWS to continue from the same point the spacecraft needs to tilt from its natural position (Fig. 15). In the latest pre-launch configuration, *Euclid* was allowed to point away from the transit meridian by tilting up to  $3^\circ$  towards the Sun and up to  $20^\circ$  away from the Sun, maximising thermo-optical stability; that is, the SAA range was restricted to  $[87^\circ; 110^\circ]$ .

If the interruption is too long, the last observed point of the EWS may no longer be visible with the allowed SAA range and can only be observed up to 6 months later, when the antipodal meridian is in transit.

Tilting from the transit meridian to another circle misaligns the FoV on the sky with respect to the orientation of the tessellation tiles. A rotation around the Z-axis (a change of AA; see Fig. 5) realigns the field with the tile. In the latest pre-launch configuration, the AA range was restricted to  $[-5^\circ; 5^\circ]$  for thermal considerations. The limitations on the range of the two solar angles, SAA and AA, together with the need to keep the fields aligned (the ‘tessellation constraint’), defines the ‘window of visibility’ (Fig. 16). The window of visibility shows the span in longitude that *Euclid* can reach away from transit, and it is a function of ecliptic latitude  $\beta$ . At low latitudes, where tilted observations do not introduce a misalignment of the FoVs, the longitude span is identical to the SAA range. Since the misalignment for a given tilt increases with latitude, the limited AA range available to align the FoVs drives the longitude span at high latitudes. Hence the window of visibility broadens towards the ecliptic equator. We note that without the tessellation constraint the ecliptic poles would have perennial visibility, and the window of visibility would broaden towards high latitudes, with the AA range playing no role in its definition. The longitude span is also directly related to how long a tile in the sky remains visible around transit.

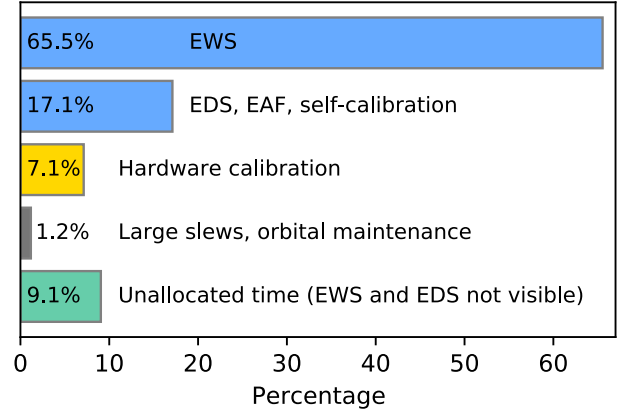


**Fig. 17.** Breakdown of activities during routine operations. The blue bars provide on-sky data that are simultaneously valuable for science, target characterisation, and calibration purposes; the instruments take additional calibration data while the data processing units are busy with the science exposures, and while the telescope is slewing. The yellow bar represents pure hardware calibration with little or no astrophysical relevance. Unallocated time arises because the survey runs out of unobserved sky areas (Sect. 4.1.2).

Tiles are observed in sequences called ‘patches’, usually covering a latitude-longitude rectangle of the RoI. The viability in scheduling a patch is closely related to the window of visibility. Tiles must be visible at all latitudes of the tessellated RoI ( $10^\circ \leq \beta < 78^\circ$ ). A reduced SAA range restricted to  $[87^\circ; 104^\circ]$  is used in practice to decrease the asymmetry of the window of visibility between high and low latitudes. Tiles must also be visible for a reasonable span of time; a longer visibility promotes wider patches.

#### 4.1.2. Unallocated time

The EWS is built by tiling patches layer by layer, starting from the poles, where the zodiacal background is lower, towards the ecliptic. The progression of the EWS also aims to observe the areas with complementary ground-based data as early as possible (Sect. 4.4). On the other hand, EWS observations must be scheduled continuously while the transit meridian scans the sky. However, longitude-wise, the area of the RoI is not uniform. At some point, the RoI area is exhausted where the Galactic plane intersects the ecliptic plane, and no EWS fields are available anymore for scheduling. This creates periods of unallocated time, all during the second half of the mission, that will then reappear regularly with a 6-month cadence, growing in duration. In the latest pre-launch configuration the unallocated time amounts to 9% of total time during routine operations (Fig. 17).

The periods of unallocated time will be used for different purposes. Foremost, they offer an opportunity for thermal decontamination of the PLM (Sect. 5.1), and to recover survey areas that were lost for example due to intermittent hardware problems, data-transmission losses, and severe space-weather events. Any remaining unallocated time not used for primary *Euclid* purposes could become available for targeted observations with the ROS, or for mini-surveys, possibly outside the RoI. Such opportunities, if any, will be developed and communicated in due time.

#### 4.2. Euclid Deep Survey

The need to calibrate and monitor the telescope, cameras and electronics requires repeated visits of specific fields that will